

# Aeroacoustic Signature of Quadrotors

Assist. Prof. Oksana Stalnov

Faculty of Aerospace Engineering

Technion - Israel Institute of Technology

Sponsored by Civil Aviation Authority of Israel (CAAI), Ministry of Transport.

This research was done in collaboration with Assure. <sup>1</sup>

<sup>1</sup>The FAAA's Center of Excellence for UAS Research. ASSURE - Alliance for System Safety of UAS through Research Excellence program

## **Notice**

This document is disseminated under the sponsorship of the Civil Aviation Authority of Israel (CAAI), Ministry of Transport in the interest of information exchange. The Government of Israel assumes no liability for the contents or use thereof.

The findings and conclusions in this report are those of the author(s) and do not necessarily represent the views of the funding authority.

This document does not constitute CAAI policy.

## Executive Summary

Urban air mobility faces increased concerns with respect to public acceptance of small scale unmanned aerial vehicles (UAVs) due to noise pollution. These vehicles, commonly referred in the literature as drones, are designed to provide thrust and torque with rotors, propellers, and fans, which are required for forward flight and/or take-off and/or landing vertically. UAVs have had a significant impact on civil and military aviation; however, noise due to rotating blades is limiting their further spread.

The high level of noise, generated during multirotor flight, is a major concern for the aeronautical industry. In the case of civil applications, noise has a more comprehensive range of implications due to the sustainability of air traffic growth. Within the scope of the Civil Aviation Authority of Israel (CAAI) research program our main objective is to collect, process and archive noise signature from a single and multiple number of propellers. The collected database can be used as basis for future definition of the required regulations for such vehicles.

The research project focuses on advancing our knowledge in understanding the acoustic signature of single and multiple propellers. The research targets acoustic measurements in static conditions in an anechoic chamber. The research plan is split into four phases: (1) perform a literature review and acquire the necessary equipment; (2) Collect and process acoustic signature of a single propellers; (3) Collect and process acoustic signature of multiple number of propellers; (4) Analysis of the acoustic data and preparation of acoustic database.

The first year of the proposed research (items (1) and (2)), has been performed successfully and exhibited very promising results. During the second year, efforts were focused on preparing the experimental setup for a four propeller configuration (items (3) and (4)). Noise suppression method, based on phase synchronization, is proposed and implemented. Experiments were performed in newly established anechoic chamber at the Technion - Israel Institute of Technology. It has been demonstrated that phase synchronization can lead to a significant noise attenuation.

# Contents

<b>1</b>	<b>Scientific Background</b>	<b>1</b>
1.1	Introduction . . . . .	1
1.2	Propeller Noise Sources . . . . .	2
1.3	UAS Noise Certification . . . . .	4
<b>2</b>	<b>Single Propeller Acoustic Signature</b>	<b>8</b>
2.1	Experimental Setup . . . . .	8
2.2	Experimental rig . . . . .	9
2.2.1	Acoustic Equipment . . . . .	9
2.2.2	Aerodynamic Equipment . . . . .	10
2.2.3	Measurement Procedure . . . . .	11
2.3	Results . . . . .	12
2.3.1	Effect of Shaft Rotational Speed . . . . .	13
2.3.2	Evaluation of the Tonal and Broadband Contributions . . . . .	13
<b>3</b>	<b>Quadrotor Acoustic Signature</b>	<b>19</b>
3.1	Experimental Apparatus . . . . .	19
3.1.1	Experimental Rig . . . . .	20
3.1.2	Free-field Measurements . . . . .	21
3.2	Results . . . . .	23
3.2.1	Implementation of Phase Control . . . . .	24
3.2.2	Aerodynamic Performance . . . . .	27
3.2.3	Acoustic signature . . . . .	27
3.3	Conclusion . . . . .	34
3.4	Future Directions . . . . .	35

<b>A Aerodynamic Model</b>	<b>37</b>
A.0.1 Blade Element . . . . .	38
A.0.2 Momentum Theory . . . . .	39
A.0.3 Derivation of BEMT . . . . .	40
A.0.4 Tip Correction Function . . . . .	43
A.0.5 Post stall Aerodynamic Database . . . . .	43
A.0.6 Convergence Algorithm . . . . .	44
A.0.7 XFOIL . . . . .	45
<b>B Aeroacoustic Model</b>	<b>47</b>

# Chapter 1

## Scientific Background

### 1.1 Introduction

Environmental noise pollution relates to noise caused by road, rail and airport traffic industries, including the unmanned aircraft sector. Global interest in small, multirotor, unmanned aerial vehicles (UAVs) and unmanned aerial systems (UASs) is rapidly growing. Currently, the number of unmanned aerial systems (UASs) being used is on the rise and experts are stating that this industry is expected to quadruple its size by 2022 [1].

Multicopters can fly horizontally and vertically, as well as, in a hover state. Because of their unique hovering ability, e.g., vertical take-off and landing, the rotary-wing UASs are very attractive for both civil and military applications. The rise in air traffic volume of this type of vehicle leads to an increase in noise pollution. Annoyance may be caused by both overall sound pressure level and specific tones in the noise spectrum. Noise pollution is currently a major issue that has to be dealt with. Noise can impact children's learning, interrupt conversations, and disturb sleep. Apart from being annoying, noise pollution can lead to severe health problems, such as hypertension, sleep deprivation and harmful cognitive effects. The European Environment Agency considers environmental noise to be more damaging to health than passive smoking.

A recent NASA study [2] has found that the buzz of a drone is more annoying to human beings than the rumble of cars and trucks, a sign that the ambitious plans of Amazon, UPS and Domino's Pizza to deliver their goods by drone, could reshape the soundscape of cities and suburbs for the worse. Above all, the motivation for this research is the European Authority EASA instructions: *'The current framework foresees regulatory limitations on noise for unmanned aircraft subject to type certification. Noise even from unmanned aircraft in the open category should be abated as much as possible'*.

Since brushless motors are relatively quiet, most of the noise originates from the rotating blades. The noise emitted by a propeller is mainly due to two components. The first is harmonic in the blade passing frequency (BPF). It is almost rigorously periodic and presents a discrete frequency spectrum. The second is a broadband and has a continuous behaviour in the frequency domain. The physical mechanism which produces the harmonic noise is related to the blade thickness and its surface aerodynamic loading.

The theoretical prediction of the harmonic noise produced by rotating blades, in particular by propellers, is classically based on the analysis of the Ffowcs-Williams Hawkings equation [3]. In principal, the amount of sound emitted by a rotary-wing is a function of the blade tip speed and blade loading. Small UASs employ fixed pitch propellers and thrust is modified with changing the motor shaft rotational speed. In practice, there are many effects that can influence the blade loading and the associated acoustic signature. The amount of sound is obviously dependent on the observer location, since the sound field is directional.

Early scientific attention has been primary focused on the deterministic component of rotor aerodynamic noise [4, 5]. This is mainly because helicopter blades have high rotor tip speeds [6], which result in high acoustic amplitudes at the BPF frequency and the associated harmonics. Therefore, these tonal components have conventionally dwarfed the contribution of broadband noise to the overall acoustic signature. However, for small-in-diameter propellers, broadband noise is a significant contributor. Recent research efforts have focused on either aerodynamic or acoustic performance of small-scale propellers. For instance, aerodynamic performance of off-the-shelf propellers were documented in great detail by Selig et al. [7, 8]; whereas acoustic performance were documented by Interatep et al. [9], Zawodny et al. [10], and Cambry et al. [11], among others. A recent study by Tinney and Sirohi [12] discusses in great detail the aerodynamic and aeroacoustic performance of drones in a hover state. The work of Stephenson [13] focuses on the limitations of acoustic measurements in an anechoic chamber. None of these studies, however, considered the link between the aerodynamic performance and acoustic signature directivity of isolated propellers with smaller-in-diameter blades, and most importantly, the corresponding separation into tonal and broadband contributions and their associated directivity and scaling.

## 1.2 Propeller Noise Sources

Design considerations, especially at smaller scales, have pushed the manufacturers to make use of electric motors for most multicopters and drones. The electrical motors are far quieter than other means of propulsion. A dominant source of noise in the propulsion system is the combination of

motor and propeller. A significant part of the noise is due to vibrations of the electric motor structure [14]. The use of electric motors makes the propeller the leading noise contributor. Propeller noise, aeroacoustical in origin, is generated due to the interactions between the flow and the rotating blades [15]. The acoustic signature of modern rotating machinery is composed of a number of sources that can be categorised into broadband noise, distributed over a very wide spectrum, and a series of superimposed discrete tones at multiples of the BPF.

Propellers consist of a number of rotating blades and produce discrete tones with an underlying broadband base level. Tonal contribution is produced mainly by the force and volume displacement effects, exerted by the fluid [16]. In an orthogonal coordinate system the resultant aerodynamic loads can be decomposed into thrust (force normal to the plane of rotation) and torque (moment within the plane of rotation). Steady loads can be represented as an array of dipole sources in the rotor disc [17]. The overall sound intensity radiated by a dipole is proportional to the sixth power of the characteristic velocity [15, 18].

In addition to experiencing the aerodynamic forces and moments, an element of air in the disc is physically moved aside by the finite thickness of the blade. In a fixed frame of reference this displacement is equivalent to a periodic introduction and removal of mass near the rotor disc. The rate of mass introduction at a point is determined by the blade's airfoil geometry, incidence, and speed. At low tip Mach numbers, however, airfoil thickness noise is generally small, compared with the noise arising from the steady and unsteady aerodynamic loads.

Propellers operating in a uniform flow with low turbulence generate broadband which is random and non-periodic in nature [19, 20]. Broadband noise is related to random aerodynamic processes and can be related to several mechanisms [21, 22, 23]. Propellers operating in a uniform flow with low turbulence generate broadband self-noise, which is random and non-periodic in nature [19, 24]. The broadband self-noise sound production in quiet, low turbulence flow, is due to interactions of a turbulent boundary layer with the trailing-edge [25, 26, 27]. Sharp edges scatter pressure fluctuations from relatively short aerodynamic waves (that do not radiate sound to the far-field) into acoustic waves [28]. In highly unsteady inflows, broadband turbulence ingestion noise is generated due to interaction of unsteady turbulence with the leading edge of the blade [29]. Turbulence ingestion noise can also produce tonal, or quasi-tonal noise, if multiple blades chop the same eddy. A recent study of Stephenson et al. [13] highlighted the significance of flow recirculation in static measurement on an isolated rotor's acoustic emissions in an anechoic chamber. Broadband noise can also be produced by a tip vortex [30, 31].

Since the diameter of a rotary-wing is in the order of half a meter (or less), there is very little information available on an aerodynamic performance and acoustic characteristics of rotors

and propellers at this scale. These vehicles tend to employ propellers which are small-in-diameter, where the chord based Reynolds number is in the order of  $10^5$  and lower, thus treading the region of fully laminar to transitional boundary layers [32, 33, 34]. Therefore, these systems are particularly sensitive to the Reynolds number effects, with degradation in aerodynamic performance at lower rotational speeds [7]. Moreover, there are many studies regarding small propeller aerodynamic performance [7, 35, 36]; fewer are available concerning noise emission from larger diameter [12, 37].

### 1.3 UAS Noise Certification

In the USA, unmanned aircraft are subject to regulation by the Federal Aviation Administration (FAA) to ensure safety of flight, and safety of people and property on the ground. The FAA's Office of Environment and Energy (AEE) is supporting the FAA Unmanned Aircraft Systems to ensure the safe, efficient, and timely integration of UASs into the United States' National Airspace System. In order to fulfil this mission, the FAA is developing standards, procedures, and regulatory products. The U.S. Department of Transportation, Research and Innovative Technology Administration, John A. Volpe National Transportation Systems Center, Environmental Measurement and Modeling Division (Volpe), is supporting the aircraft noise certification initiatives of the Federal Aviation Administration (FAA), Office of Environment and Energy. The Volpe Center Environmental Measurement and Modeling Division provides support to FAA's AEE by performing validation of audio measurement, recording and analysis systems, whether fully-integrated or comprised of individual off-the-shelf components used by noise certification applicants.

The primary control over aircraft source noise is the noise certification process, which is the responsibility of the AEE within the FAA. States and local jurisdictions are increasingly exploring regulation of unmanned aircraft systems or proceeding to enact legislation relating to unmanned aircraft systems operations. Public comments on the FAA proposed rule, 'Operation and Certification of Small Unmanned Aircraft Systems' (Docket No. FAA-2015-0150), expressed concern about the possible impact of state and local laws on UAS operations.

Noise certification refers to the process by which the aircraft manufacturer has to demonstrate that his product meets basic noise standards, in the same way that it has to meet safety standards before it can enter commercial service. For each new aircraft the aircraft manufacturer obtains noise certification by demonstrating that noise levels comply with the limits specified in the regulations. A specific Type Certificate or a type Certificate Data Sheet for Noise (EASA TCDSN) is appended to the Aircraft Type Certificate.

There are currently three prime sets of regulations specifying in particular the maximum noise

limits to be complied with and the compliance demonstration methods to be used:

1. ICAO Annex 16 (Environmental Protection, Volume I — Aircraft Noise), the only internationally acknowledge regulations.
2. EASA: Commission Regulation (EC) No 1702/2003 – Part 21 (was JAR 36) for Europe.
3. FAR Part 36 for the United States.

International Civil Aviation Organisation (ICAO) Standards (related to noise) are contained in Annex 16 to the 1944 Convention on International Civil Aviation (the Chicago Convention) – Volume 1, Part II, which describes and specifies the certification procedures and noise limits for jet, propeller powered airplanes and rotorcraft. Federal aviation regulation (FAR) 36 specifies the type of testing, measurement procedures, and subsequent calculations which must be made and submitted in order to certify an aircraft. FAR 36 for helicopter testing specifies three flight modes for acoustic testing: take-off, flyover, and approach. These standards apply to new type of helicopters and are consistent with ICAO Annex 16 (Volume 1 Chapter 8 and Chapter 11).

Noise Standards for helicopters were first included in Annex 16 in 1981. Currently, the Standards applicable to helicopters are contained in the Chapters 8 and 11 from Annex 16 Volume I. Chapter 8 is applicable to all helicopter types, whereas Chapter 11 provides an optional simplified certification procedure for light helicopters with a maximum certificated take-off mass of 3,175 kg (or less). Recently (in 2014) the ICAO Council adopted noise Standards for tiltrotors, which were included in Chapter 13 of (Annex 16 Volume 1). The Standards set aircraft noise limits as a direct function of Maximum Take-off mass. Currently, none of the above discussed Standards discusses noise of UAS.

The most frequently used metrics include:

1. EPNL – effective perceived noise level with tone and duration corrections.
2. SEL – equivalent continuous A-weighted sound pressure level; this is a dB(A) based unit that accounts for duration in the same manner as EPNL, but without discrete tone correction.
3. DNL – day/night equivalent sound level; their energy is averaged over 24 hours and night time events are weighted by adding 10 dB(A).
4. DEN – day/evening/night sound level, with 5dB(A) added weighting for evening period.

The UASs are designed to operate within urban environments, potentially exposing communities to significant levels of tonal and broadband noise. Current noise certification requirements, for

fixed- and rotary-wing aircraft, may not adequately capture the noise effects of UASs. The only completed regulation that covers sUAS is 14 CFR part 107. The sUAS rule includes the option to apply for a certificate of waiver, which allows for a UASs operation (under 55 pounds) to deviate from certain operating rules, if the FAA finds that the proposed operation can be performed safely under the terms of a waiver.

There are several Roadmaps aimed at integrating UASs into civil and military airspace over the coming years. Circular 328 from the International Civil Aviation Organization (ICAO) makes note of the possibility that noise from many UAS sources could become a problem in the future: ‘As new products and aircraft come into use, it may become apparent that additional noise and emission standards are necessary’. The FAA UAS Roadmap has yet to include a section on UAS noise. The Remotely Piloted Aircraft Systems Roadmap also touches on the potential for noise issues in future, but focuses on the fact that their use in commercial applications may be more beneficial than current nonelectric aircraft. This forethought shows that the governing agencies are beginning to consider noise standards for UAS.

Currently, with the fairly limited regulation of UAS, particularly with respect to noise, it seems that the most restrictive regulations may be those presented by the Environment Protection Authority (EPA), or the equivalent body in each respective country (for example, the European Environment Agency in Europe). These regulations vary between countries, states, and areas. Most EPA regulations prohibit noise from electrical equipment (which would include electric UAS) outside daylight hours (before 7 a.m. and after 8 p.m.) most days. As the use of UAS becomes more and more accessible, people will more commonly use them in their backyards, which can be a nuisance to neighbours.

UAS have the potential to alter the community soundscape due to their noise characteristics that are qualitatively different from traditional aircraft. The challenge with determining what is considered to be an ‘unreasonable’ noise level is that the perception of noise is subjective. There are many different noise metrics that can be used to express the noise exposure. The human ear sensitivity depends on the frequency of the sound. Noise levels are often measured in the frequency range from 50 to 10,000 Hz, where noise levels lower than 50 Hz are usually not generated by an aircraft and impose little of annoyance for human beings (relative to other frequencies). The situation is different when UASs are considered, since the typical blade passing frequency of a propeller is at low frequency range.

Regulators are beginning to address the environmental impact of drones on communities, including noise pollution. Therefore, a fair and accurate method of determining the community annoyance needs to be determined. This begins with correctly estimating the noise of small-in-

a-diameter propellers in anechoic environment. To date, there is very little scientific research on the human impacts of noise from UAS, although there have been increased efforts to measure and model the noise generated by them and their components. Within the scope of the report, A-weighting (see International standard IEC 61672:2003) is applied to the measured sound pressure levels in an effort to account for the relative loudness perceived by the human ear, as the ear is less sensitive to low audio frequencies.

Under the agreement between the Government of the United States of America and the Government of Israel for promotion of Aviation Safety, the government of Israel follows the noise certification requirements under the FAA regulations. The regulatory basis of UAVs fall under the certification requirements for helicopter.

## Chapter 2

# Single Propeller Acoustic Signature

### 2.1 Experimental Setup

To minimise interference from the background noise, the experiments were performed in a fully anechoic chamber at Dynamica Design Ltd.(IL). The physical size of the chamber is  $4.8\text{ m} \times 4.3\text{ m} \times 3.6\text{ m}$ . The walls of the chamber are acoustically treated with glass fiber wedges to approximate free field conditions above a cut-off frequency of 150 Hz. At frequencies above the cut-off, background noise level in the facility is low, and in the anechoic chamber where experiments were conducted, this level is about 15 dB.



Figure 2.1: Propeller rig in the anechoic chamber. The encoder is positioned below the motor shaft and the ATI Mini40 load sensor is placed under the encoder.

## 2.2 Experimental rig

A propeller and motor combination were mounted on a cylindrical strut at a height of about 1 m above the ground. The support is small in diameter, compared to the motor, in order to minimise interference with the propeller's wake. The UAV propeller was powered using a brushless electric motor and castle creations phoenix electronic speed controller (ESC). The power source is a standard power supply. The motor's rotational speed per minute (RPM) was set using a pulse width modulation (PWM) signal, that can be either manually set or generated by the NI PXIe-6341 card. A PWM signal is a pulsed signal, at a frequency of 50 Hz. The motor's angular velocity is based on the pulse width. Note that the pulse width is interchangeable with the signal's duty cycle, which is the percentage of time that the signal is in the high position out of the whole period. The PWM signal is sent to the ESC, which regulates the current to the motor, based on the commands that it receives.

The acoustic signature was acquired using the 24 bit NI PXIe-4497 card, while the NI PXIe-6341 card is used to acquire both the load sensor and the encoder signals. Synchronisation between the cards is accomplished in the software (LabVIEW) by setting the clock of the PXIe-4497 card as a master and the PXIe-6341 card as the slave in a NI PXIe-1082 chassis. The acoustic and aerodynamic data were collected simultaneously at a sampling rate of  $F_s = 40$  kHz for a period of  $T_s = 20$  s.

### 2.2.1 Acoustic Equipment

The sound pressure in the free field were measured by an array, consisting of eight 46AE G.R.A.S. IEPE-powered half inch free field condenser microphones, distributed over a circular arc. These microphones, with matching pre-amplifiers (model 26CA), have a nominal frequency response range of 5 Hz to 10 kHz ( $\pm 1$  dB accuracy) or 3.15 Hz to 20 kHz ( $\pm 2$  dB accuracy), as well as a dynamic range of 17 dB to 138 dB with nominal sensitivity of 50 mV/Pa. The integrated Electronic Piezo-Electric (IEPE) power is provided by the NI PXI-4497 card.

The microphones were placed symmetrically around the propeller hub at radial distance of 1.5 m, and span an angular range of  $0^\circ < \theta < 105^\circ$ . An illustration of this set-up is shown in **Figure 2.2**. For a nominal propeller geometry with diameter  $D = 14''$  (corresponding to  $D = 0.35$  m), a distance of more than  $4D$  was chosen since it is considered the far field in the literature [12]. In the near field, turbulence levels can be high, thus affecting acoustic measurements. Microphones were placed at constant angular increments of  $\Delta\theta = 15^\circ$ , starting above the propeller's hub (corresponding to  $\theta = 0^\circ$ ), and reaching a position of up to  $105^\circ$ . The arc array is such that  $\theta = 90^\circ$  is

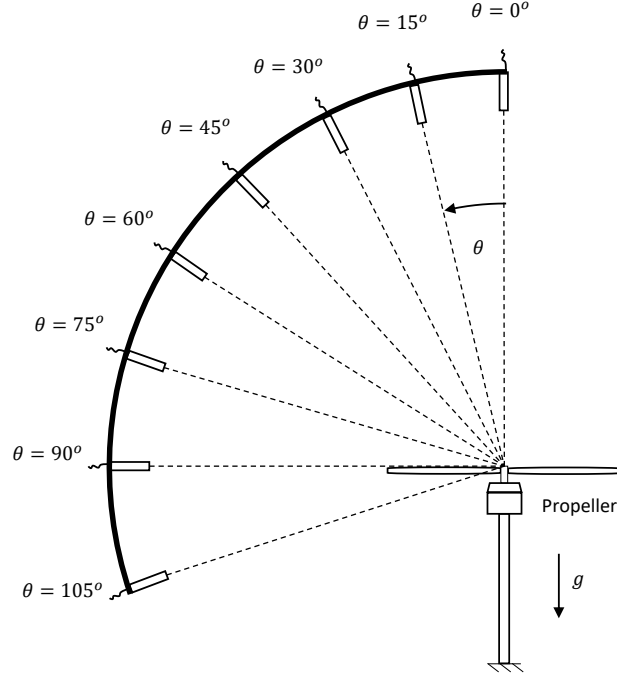


Figure 2.2: Schematic description of the microphone observer position with respect to the propeller's plane of rotation.

at the rotor disk plane, with  $\theta = 0^\circ$  being measured in the direction of the thrust vector. With this arrangement six microphones are placed in varying angles above the propeller's plane, one within its plane, and one under the rotation plane.

The microphones were calibrated *in-situ* using a B&K 4231 sound calibrator at a frequency of 1 kHz and sound pressure level of 94 dB. The accuracy in the Class-1 microphone sound pressure level measurements is 1 dB (as indicated by the manufacturer). These calibrator conforms to EN/IEC 60942 Class LS and Class 1, and ANSI S1.40-1984.

### 2.2.2 Aerodynamic Equipment

During the measurements, the ATI Mini40 load sensor was mounted beneath the motor. This strain-gauge-based load cell can measure three orthogonal forces and moments. The axial direction, which is of interest when considering propellers, is the vertical direction, and is perpendicular to the load sensor's top and bottom surfaces ( $Z$ ). Two additional directions are  $X$  and  $Y$ , which are both side forces, parallel to the load sensor's top and bottom surfaces and perpendicular to each other and to the axis. The sensor allows measurement of thrust and torque, which correspond to the force  $F_z$  and moment  $M_z$ , respectively. The load cell was manufacturer calibrated to a full-scale  $F_z$  of 60 N and a full-scale torque  $M_z$  of 1 Nm. The coordinate system is shown in the

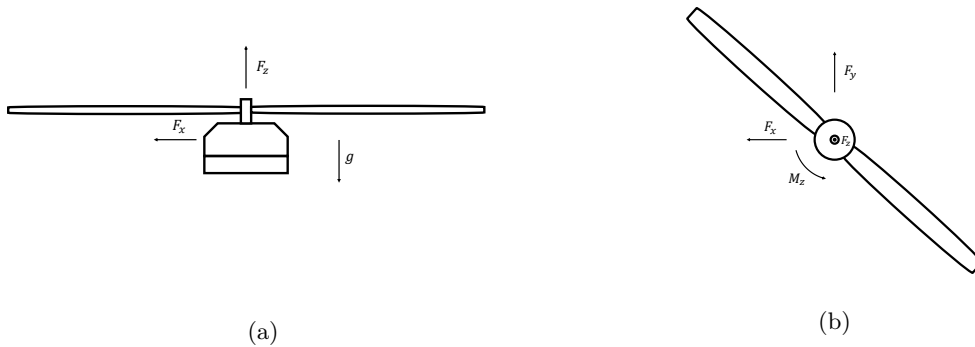


Figure 2.3: Coordinate system (a) side and (b) top view.

diagram in **Figure 2.3**.

Within the scope of the study, a range off-the-shelf fixed pitch APC Thin Electric propeller geometries were studied. The nominal geometry is a two-bladed APC Thin Electric  $14 \times 10$  propeller, which is often used in UAVs. When describing a propeller geometry a diameter times the pitch (in units of inch) is often used. The main consideration when choosing a reference propeller was the availability of published aerodynamic data, so as to have a point of comparison. While data concerning the acoustic signature of small UAV propellers are scarce, Brandt and Selig’s work [7] contains data concerning the aerodynamic performance of a range of small-in-diameter propellers, and a database with all of the collected data is available online [8].

### 2.2.3 Measurement Procedure

Following the measurements, the raw data was post-processed to evaluate the performance. The aerodynamic and aeroacoustic measurements were collected simultaneously. Discussion of the results is separated into tonal and broadband contributions to the spectra. To evaluate the sound pressure level at certain frequencies, digitized time domain acoustic signals were converted into engineering units and transformed into frequency domain using a Fourier Transformation. The data was partitioned into blocks and then averaged in the frequency domain. The narrow-band spectra were estimated using Welch’s averaged modified periodogram method with a window of  $2^{13}$  samples in size, and 50% overlap, resulting in a bandwidth of about 4.5 Hz.

The tonal and broadband behaviour can be better observed by integrating the contributions and plotting the overall sound pressure level in a band (or *BSPL*). The *BSPL* is estimated according to accepted standards in the acoustic community, i.e. sound pressure level in a band

$$BSPL = 10 \log_{10} \left( \frac{S_{pp}}{p_{\text{ref}}^2} \right) \quad (2.1)$$

with

$$S_{pp} = \int_{f_1}^{f_2} \overline{p^2}(f) df \quad (2.2)$$

where  $f_1$  and  $f_2$  denote the lower and upper frequency limits within which the band sound pressure level is evaluated. Here the standard reference pressure of  $p_{\text{ref.}} = 20 \mu\text{Pa}$  is used.

Corrections for human ear effects are important in this study and are achieved using the A-weighting standard described by the International Organization for Standardization (ISO 226:2003). The A-weighting is the standard weighting for outdoor community noise measurements. The A-weighting was applied during the post-processing of the measured data in MATLAB software using the following weighting function to ensure the normalisation to 0 dB at 1kHz

$$A(f) = 20 \log_{10}(R_A(f)) + 2$$

where

$$R_A(f) = \frac{12194^2 f^4}{(f^2 + 20.6^2) \sqrt{(f^2 + 107.7^2)(f^2 + 737.9^2)(f^2 + 12194^2)}}$$

The weighting function  $R_A$  is applied to the amplitude spectrum of the unweighted sound level. The A-weighting was designed to follow the 40 phon curve and used for measuring sounds of low intensity.

## 2.3 Results

Within the scope of the Civil Aviation Authority of Israel research program, acoustic signature of a range of off-the-shelf APC Thin Electric propeller geometries was studied systematically in an anechoic environment. The acoustic signature of a propeller is a combination of various aerodynamically generated sources. Efforts were made to understand the acoustic signature of the propellers in a hover state.

Acoustic measurements were conducted with an arc of free field microphones at a radial distance of  $r = 1.5\text{ m}$  from the propeller hub. The acoustic measurements were complemented with simultaneous measurements of aerodynamic forces and moments. To allow independent monitoring of the motor shaft rotational speed, a magnetic encoder was installed under the motor shaft. During the experiments in the anechoic chamber, the UAV propeller was operated in a hover state, which is a unique flight condition that the blade experiences during vertical take-off and landing. When operated at hover, the thrust generated by the propeller should be equal to the vehicle's weight.

### 2.3.1 Effect of Shaft Rotational Speed

We commence our report by examining the effects of shaft rotational speed on the acoustic signature of the APC Thin Electric  $14 \times 10$  propeller. Measurements were performed at rotational speeds ranging between 2000 and 4500 RPM, in increments of 250 RPM. Within this range of rotational speeds, the motor and the ESC were operated within their thermal limits.

**Figure 2.4** shows a typical far field sound pressure level (*SPL*) frequency spectra of the APC Thin Electric  $14 \times 10$  propeller at three microphone observer positions, i.e.,  $\theta = 90^\circ$ ,  $\theta = 45^\circ$  and  $\theta = 0^\circ$ . For clarity, sound pressure level acoustic data are shown in increments of shaft rotational speed of 500 RPM. The grey dashed line shows the facility's background noise level. The corresponding A-weighted spectra, which account for the human perception of noise, is shown in **Figure 2.5**. Above the chamber cut-off frequency of 150 Hz, a difference of at least 10 dB is observed at both tonal and broadband components. Below the cut-off frequency, the tonal contribution at the BPF is at least 10 dB higher than the noise levels of the facility's background. The caveat is that lower-frequency sound waves, comprising longer wavelengths, are less susceptible to atmospheric absorption, and will propagate farther away from the source. The propeller acoustic signature is characterised by a series of discrete tones with an underlying broadband base level. The spectrum is visibly dominated by the tonal noise components at the BPF and its harmonics. The tonal noise contribution shows up in the low frequency range, whereas the high frequency range is dominated by the broadband contribution.

The fundamental BPF frequency is a product of the propeller rotational speed and the number of blades. For a two-bladed propeller, this frequency is twice that of the motor shaft rotational speed, e.g., for the rotational speed of 3500 RPM the BPF can be calculated as  $f_{BPF} = 3500/60 \times 2 = 117$  Hz, where 2 corresponds to the number of blades. As expected, with an increase in propeller shaft rotational speed, the tonal noise contribution increases in terms of both the sound pressure level and frequency. The broadband noise level also increases with the increase in rotational speed, but only up to a certain point. Above 3500 RPM, the noise levels stop rising and the trend changes.

### 2.3.2 Evaluation of the Tonal and Broadband Contributions

As previously indicated, the project focuses on advancing our knowledge in understanding the acoustic signature of single and multiple propellers. Therefore, in evaluation of the tonal and broadband contributions in a band A-weighting was not applied since A-weighting is frequency dependent.

The following tonal and broadband ranges were selected to allow a quantitative comparison:

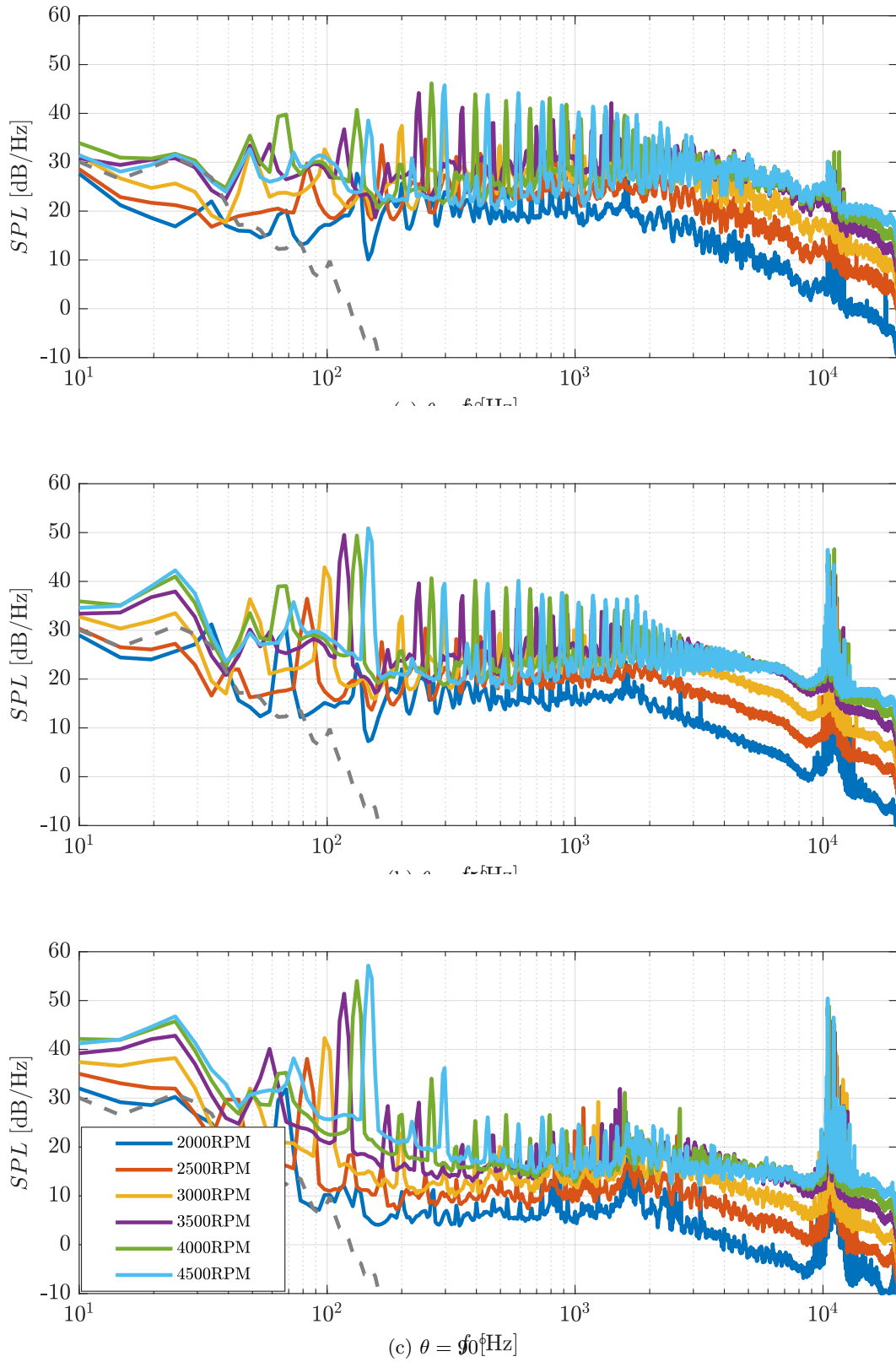


Figure 2.4: *SPL* frequency spectra (ref.  $20\mu\text{Pa}$ ) of the APC Thin Electric  $14 \times 10$  propeller at three microphone observer positions. The grey dashed line shows the background facility noise level in the anechoic chamber.

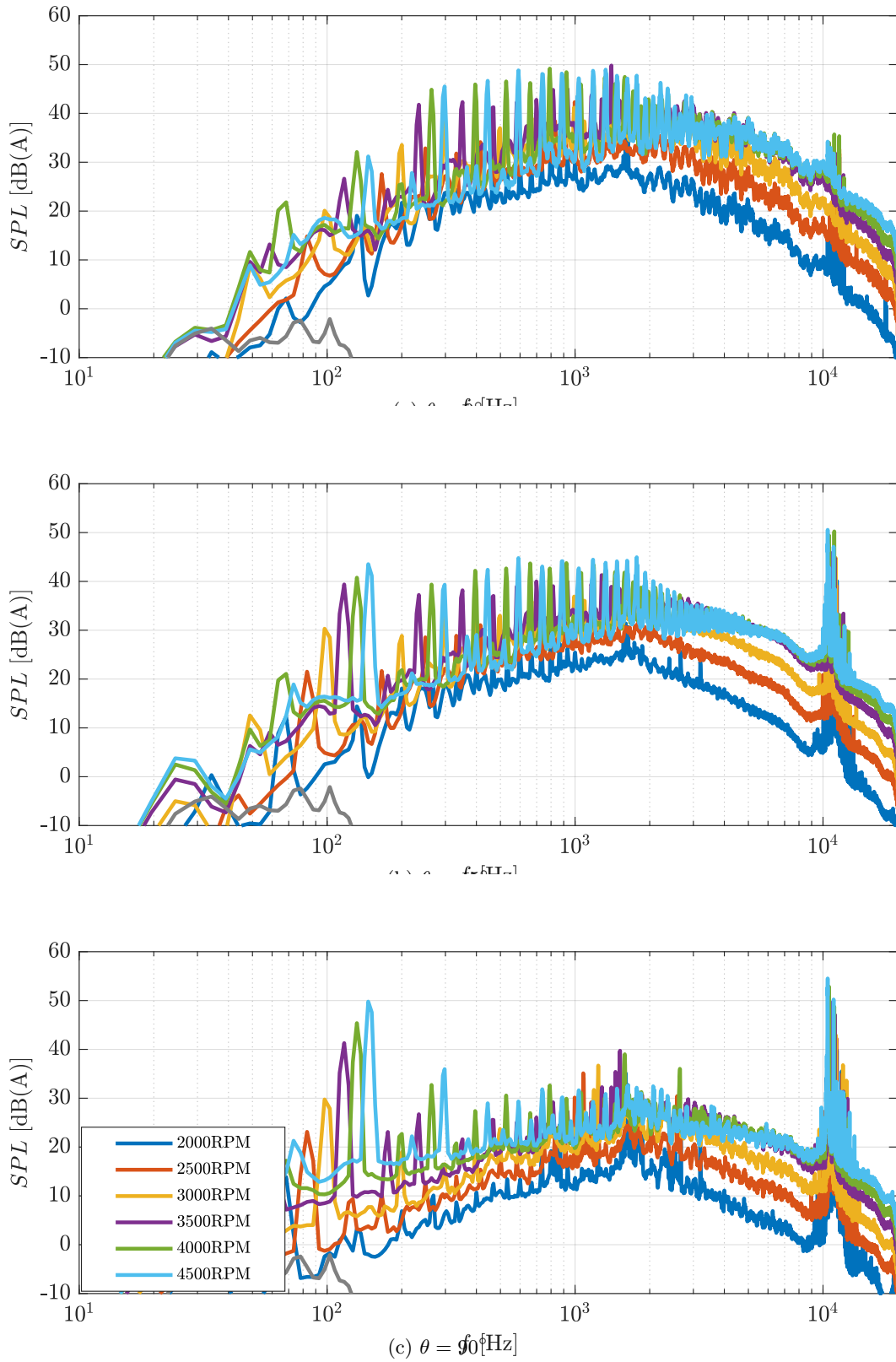


Figure 2.5: A-weighting  $SPL$  frequency spectra (ref.  $20\mu\text{Pa}$ ) of the APC Thin Electric  $14 \times 10$  propeller at three microphone observer positions. The grey dashed line shows the background facility noise level in the anechoic chamber.

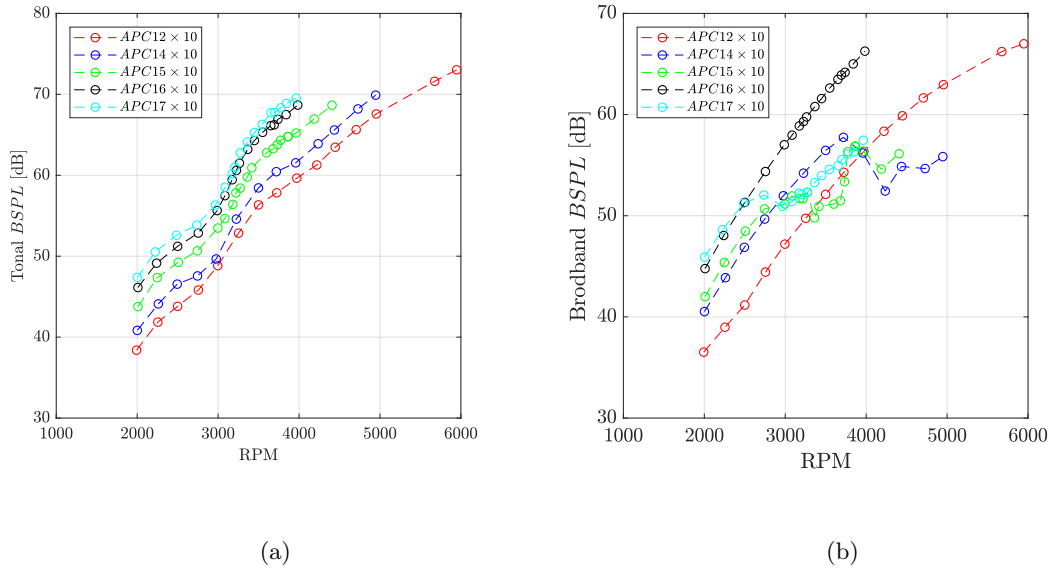


Figure 2.6: (a) Tonal and (b) broadband  $BSPL$  as a function of rotational speed for propellers with varying diameters as recorded microphone positioned at  $\theta = 90^\circ$ .

1. The first frequency bandwidth is in the low frequency range around the propeller's BPF. This range corresponds to frequencies where the tonal component dominates the noise spectrum, and was different for each measurement depending on the motor angular velocity. A frequency range of  $\pm 15$  Hz around the BPF was chosen for the integration.
2. The second frequency bandwidth corresponds to broadband in the range of 3-7 kHz.

The bands where motor noise is prominent are not affected by its angular velocity, and, therefore, the same broadband range was selected. Tonal noise contribution was calculated in a 30 Hz band centered at the main (or first) BPF. Sinibaldi and Marino [38] pointed out that the acoustic behaviour of the motor changes when it is loaded with the propeller, meaning that the measurements of the motor noise do not necessarily give an accurate picture of its contribution to the propeller's acoustic signature, but that it does give an assessment of this contribution. Comparable results for motor noise were also obtained by Intaratep et al. [9], who showed similar noise levels at a slightly wider frequency band to those obtained here. This suggests that the noise signature of a motor is not universal and should be documented when propeller noise is being investigated.

To determine the effects of the propeller diameter, off-the-shelf APC Thin Electric propellers were used. Due to motor limitations, the range of motor shaft rotational speeds was varied between propellers. In certain rotational speed ranges, the rotational speed resolution was increased (data were recorded every 100 RPM) to better observe variations in the acoustic signature.

The  $BSPL$  was calculated in the same frequency bands that were previously used with the

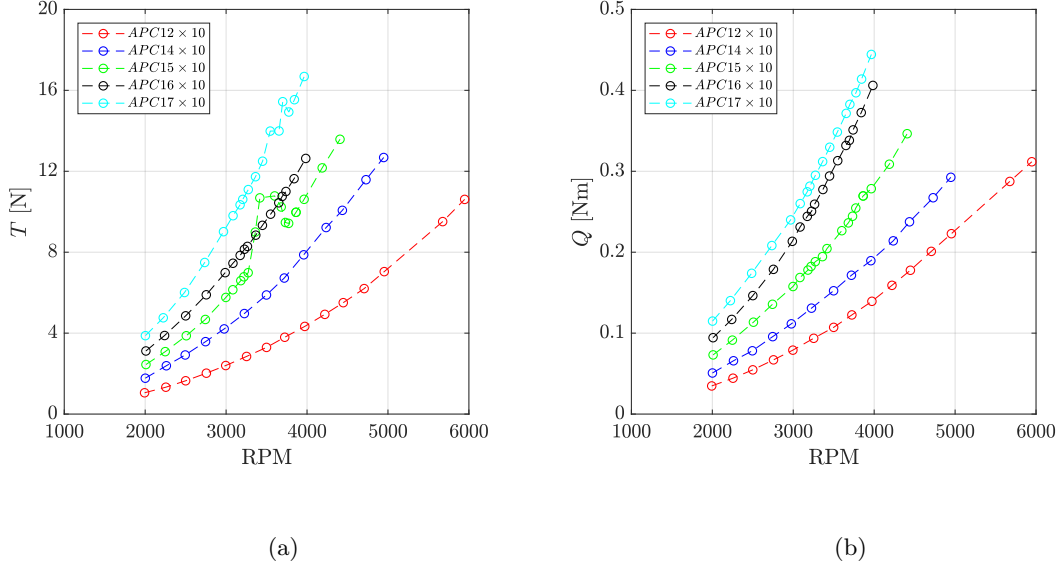
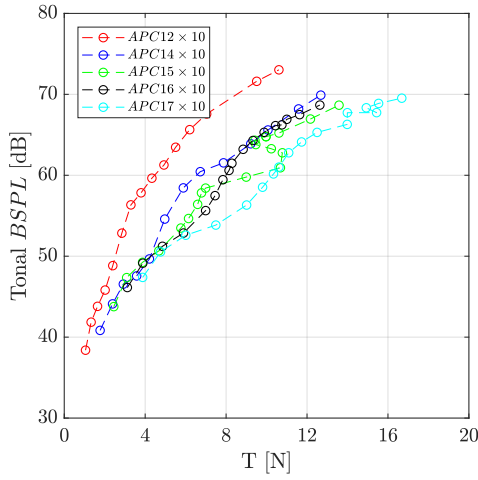


Figure 2.7: (a) Thrust and (b) torque as a function of motor shaft rotational speed.

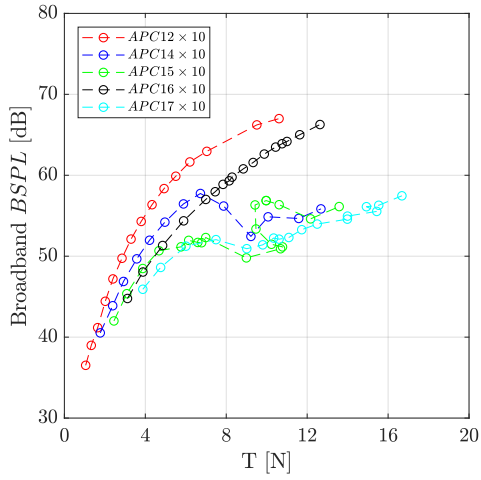
APC Thin Electric 14 × 10 propeller for both the tonal and broadband components. **Figure 2.6** shows the tonal and broadband contributions as a function of the motor shaft rotational speed at the microphone observer position of  $\theta = 90^\circ$ . Tonal contribution exhibits similar trends to those observed with the nominal geometry. For a given motor shaft rotational speed, higher sound pressure levels are observed with the 17 × 10 propeller geometry and lower sound pressure levels with the 12 × 10 propeller geometry. Broadband noise also shows a similar behaviour when observing lower RPMs, broadband noise sound pressure level continues to increase as the rotational speed increases.

The thrust and torque that are exerted by a propeller are a function of its diameter and motor shaft rotational speed (see **Figure 2.7**). As expected, at a given rotational speed the aerodynamic loads increase with the increase in propeller diameter. The mean thrust shows a quadratic trend with the rotational speed. According to momentum theory, the thrust generated by a propeller is proportional to the velocity squared.

Since aerodynamic loads were acquired simultaneously with the far-field acoustic signature, it is beneficial to plot the  $BSPL$  as a function of the aerodynamic loads. **Figure 2.8** shows the tonal and broadband  $BSPL$  as a function of thrust. By observing the acoustic signature as a function of aerodynamic performance, it is evident that for a given thrust, the propeller with a smaller diameter (APC Thin Electric 12 × 10) is less acoustically effective than the larger propeller geometries, giving higher sound pressure levels for a given level of thrust. This effect can be attributed to the fact that the noise emission is a function of the Mach number, which is a direct



(a)



(b)

Figure 2.8: (a) Tonal and (b) broadband  $BSPL$  as a function of thrust as recorded by the microphone observer positioned at  $\theta = 90^\circ$ .

result of the propeller's rotational speed. Note that due to broadband noise reduction at higher RPMs, the  $14 \times 10$  propeller becomes more effective than the  $17 \times 10$  propeller when operated at these speeds. Intaratep et al. [9] studied aerodynamic and acoustic performance at a range of rotor geometries with diameters of about 9.5 in. They observed a wide variation of overall sound pressure levels (OASPL) as a function of thrust, which suggested sensitivity to the blade geometry. They did not, however, divide their study into tonal and broadband contributions to the acoustic signature.

## Chapter 3

# Quadrotor Acoustic Signature

With a four propeller rig, experiments were conducted in a newly established anechoic chamber at the Faculty of Aerospace Engineering, at the Technion - Israel Institute of Technology. The facility is designed to have dual use, as full anechoic chamber (AC) and as closed-return anechoic wind tunnel (AWT). The chamber is operational, whereas the anechoic wind tunnel is still under construction.

### 3.1 Experimental Apparatus

The AWT is designed for low-speed (subsonic) aerodynamic and aeroacoustic studies in the flow speed range of 10–70 m/s with a turbulence level less than 0.05%. To allow simultaneous noise and flow measurements, the AC surrounds the AWT test section. The purpose of the AC is to determine the acoustic signature of a given test article. The AC allows precise sound pressure measurements in a free-field acoustic environment. The AC is designed in a manner that allows sealing all the apertures, for conversion to a fully anechoic chamber, maintaining or exceeding the frequency cut-off of 150 Hz and background noise level of 15 dB(L) at the free-field range. The size of the anechoic chamber is 7m (length) by 5m (height) by 5m (width). Layout of the AWT/AC facility with wind tunnel components is shown on Figure 3.1.

The AC incorporates apertures for the wind tunnel contraction nozzle, collector/diffuser, and acoustic access door. An appropriate enclosure for the wind tunnel apertures is included in the design, which ensures that the room can be converted to a fully AC. The chamber is constructed as a room within a room (double wall) to reduce both air- and structure-borne noise. The internal room is placed on an appropriate vibration isolation floor. The inner room floor sets on a series of anti-vibration mounts. The double-wall structure with vibration isolation provides isolation from

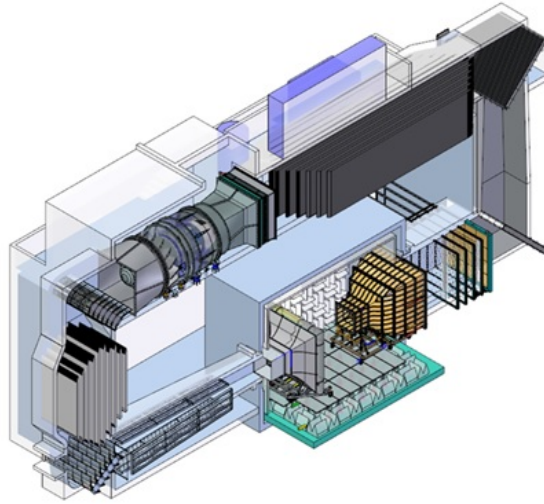


Figure 3.1: Schematic layout of the anechoic wind tunnel with an anechoic chamber at the Faculty of Aerospace Engineering, at Technion.

the main building structure. The internal walls, including the floor and ceiling of the anechoic chamber, are covered with highly absorptive anechoic wedges (manufactured from fiberglass) to provide a sound absorption level of 99% or more, down to a nominal cut-off frequency of 150 Hz. Figure 3.2 shows preliminary comparison between the anechoic chamber at the Dynamica Design Ltd. and the Faculty of Aerospace Engineering at the Technion-IIT.

### 3.1.1 Experimental Rig

To allow acoustic signature of the four propellers, a dedicated measurement stand was designed and constructed. The propellers with their motors were mounted on cylindrical struts at a height of about 1 m above the ground level at the chamber. The rig in the anechoic chamber is shown in Figure 3.3. This support structure was small in diameter, compared to the diameter of the motors, in order to minimise aerodynamic interference with the propeller's wakes. The propellers were powered by a brush-less electric motor (T motor MN 505 S - KV 320) and electronic speed controllers (T Motor ALPHA 60A HV). The stand has two rotors rotating clockwise and the other two rotating counterclockwise. The motor's rotational speed was measured in revolutions per minute (RPM). The controller input was set using a Pulse Width Modulation (PWM) signal via MATLAB. The PWM signal is a pulsed signal, with a frequency of 50 Hz, which alternates between 0 V and 1 V, where the motor's angular velocity is based on the pulse's width. Note that the pulse width is interchangeable with the signal's duty cycle. The PWM signal is sent to the ESC, which regulates the current to the motor.

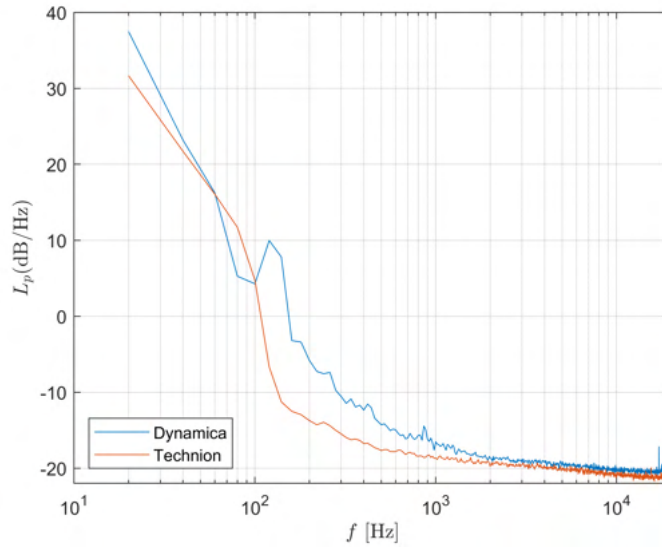


Figure 3.2: Preliminary comparison of narrowband sound pressure level between the newly established AC at the Faculty of Aerospace Engineering, at Technion and an existing chamber at Dynamica Design Ltd.

### 3.1.2 Free-field Measurements

Propeller acoustic signature and encoder signals were acquired simultaneously with 24-bit NI PXIe-4497 cards. Synchronization between the data acquisition cards was accomplished in the software by setting the clock of the cards. Data was collected simultaneously for a period of  $T_s = 60$  s. To allow background noise level measurements the recording commenced prior to the operation. To allow real time operation, data acquisition was performed with  $\Delta T_S = 0.1$  s blocks. The far-field sound pressure signature was acquired with a microphone array, consisting of 15 free-field half-inch condenser microphones, distributed over a circular arc at a radial distance of about 1.5 m from the rig center.

Given the dynamic range of the sound pressure levels produced by the propellers, as well as, the bandwidths of interest, eight 46AE G.R.A.S. IEPE-powered half-inch free-field and seven 4189 B&K IEPE-powered microphones are selected. All the microphones are type I. For instance, the G.R.A.S. microphones, with matching pre-amplifiers (model 26CA), have a nominal frequency response range of 5 Hz to 10 kHz ( $\pm 1$  dB accuracy) or 3.15 Hz to 20 kHz ( $\pm 2$  dB accuracy), as well as a dynamic range of 17 dB(A) to 138 dB with nominal sensitivity of 50 mV/Pa. IEPE power was provided by a 24 bit NI PXI-4497 card. The microphones were calibrated *in-situ* using a B&K 4231 Sound Calibrator at a frequency of 1 kHz and sound pressure level of 94 dB. The accuracy with the Class-1 microphone sound pressure level measurements is 1 dB (as indicated by the manufacturer). The calibrator conforms to EN/IEC 60942 Class LS (Laboratory Standard) and Class 1, and ANSI

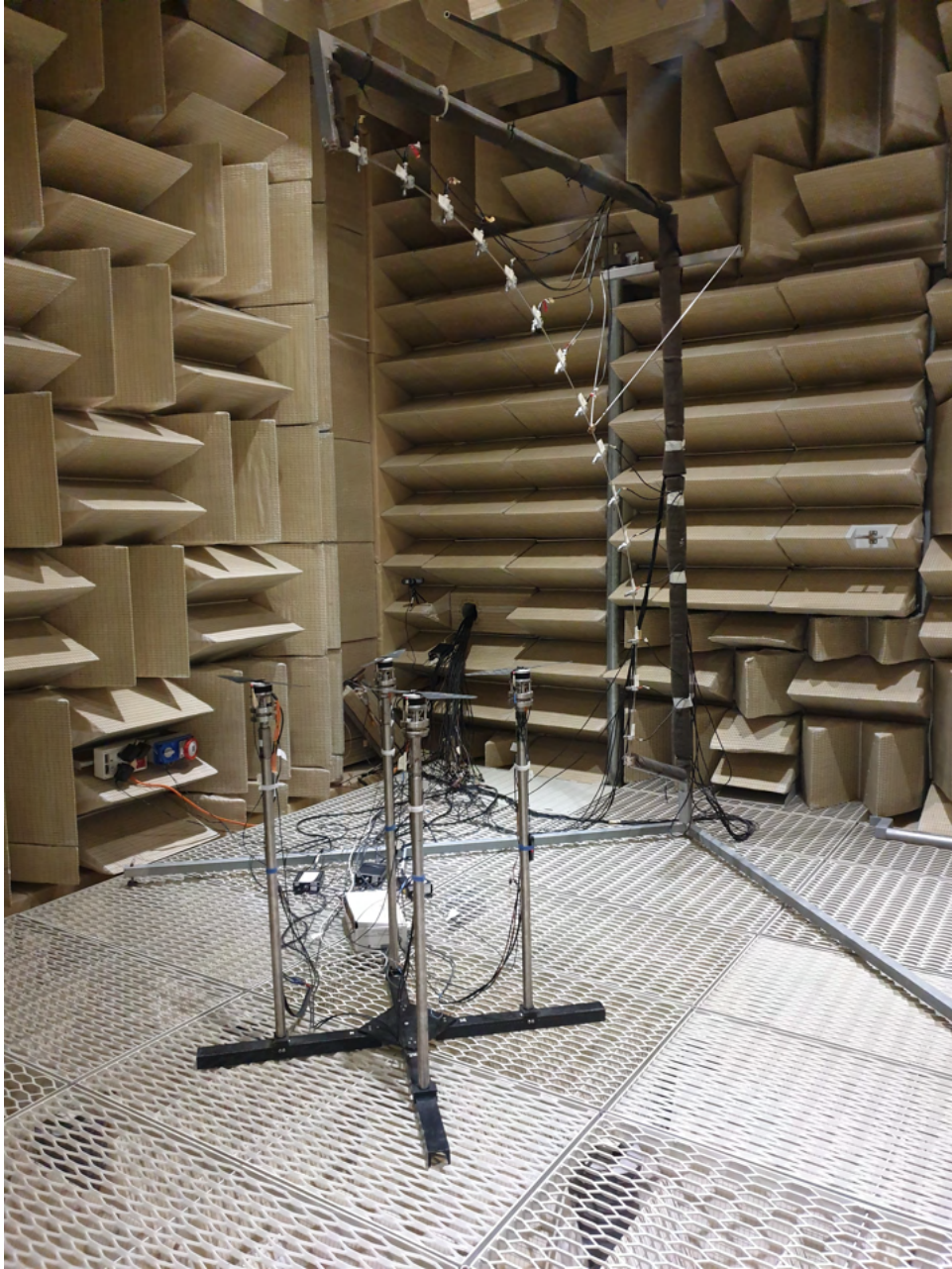


Figure 3.3: Photograph of the four rotor experimental rig in the anechoic chamber at the Faculty of Aerospace Engineering, Technon - IIT.

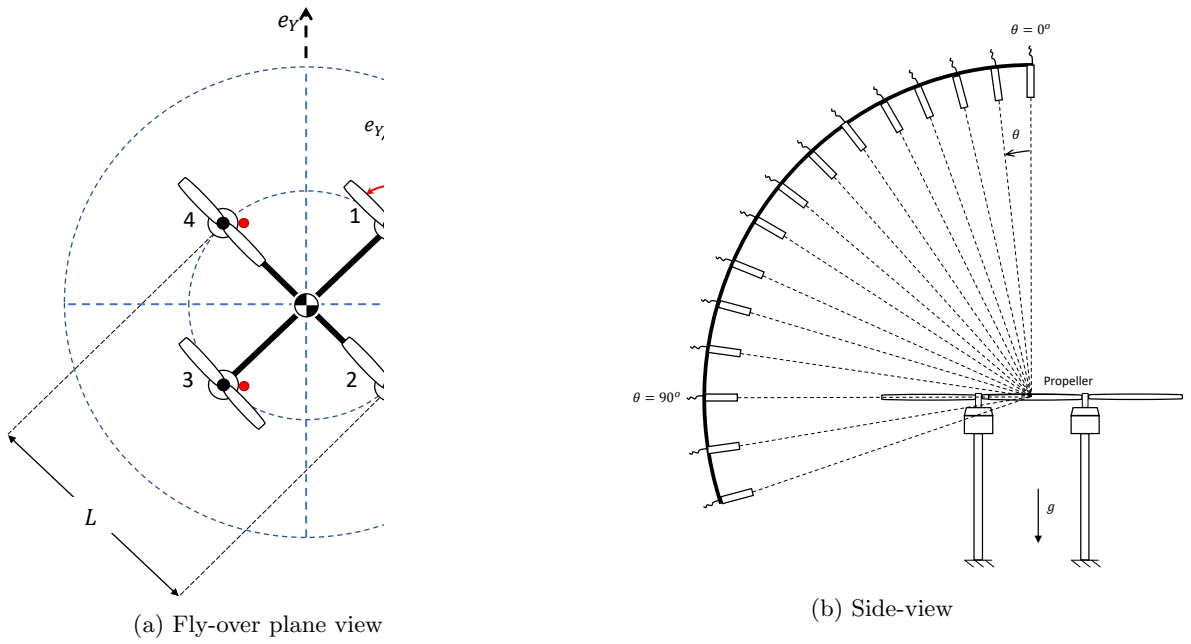


Figure 3.4: Schematic description of experimental set-up. Red dots in Figure 3.4a indicate the physical location of the optic encoder, with respect to the coordinate system. 3.4b Side view of the experimental rig shows only two rotors (out of four).

S1.40-1984.

All acoustic data were corrected to about 1.5m assuming spherical spreading. Tinney and Sirohi [12] showed that 1.5m is in the acoustic far-field for a single UAV propeller of a similar size and that spherical spreading is a valid assumption. Reflective surfaces were covered with acoustic absorbing material to minimize reflections. The noise measurement results are presented in terms of the frequency-dependent energy content of the pressure fluctuations. The power spectral density of the pressure fluctuations is estimated by using the Welch's method [39], where the data from the transducers are segmented with 50% overlap and windowed by the Hanning function.

## 3.2 Results

The basic architecture of a drone is made of four co-planar rotors (see figure 3.4a), the centers of which are at the corners of a square. This makes the blade-tip radius  $R_T$  and either the rotor-to-rotor axis distance  $L$  or the center-to-rotor axis distance  $D/2$  first parameters of interest. The rotors are assumed to radiate sound into the free-field. In current set-up the sound scattering by the quadrotor structure is not present.

### 3.2.1 Implementation of Phase Control

A phase tracking method, based on Hilbert transform (HT), is applied to detect the azimuth angle of a static rotor  $i$ . To demonstrate the phase control algorithm, it is essential to extract any information regarding the angular position along the experiment of each rotor. Therefore, the data from the optic and magnetic encoders was used to determine the angular position.

A common practice in extracting the amplitude and phase of an input signal  $s(t)$  is based on application of the HT. The transform provides proper estimate of the instantaneous phase of signal  $s(t)$  with slowly varying amplitude and frequency. The time domain techniques based on the transform allows a direct extraction of linear and nonlinear system parameters from a measured time signal. The proposed method determines instantaneous parameters even when the input signal consists of a high sweep-rate oscillating signal [40]. The HT function defines as follows:

$$\hat{s}(t)H[s(t)] = \frac{1}{\pi} \int_{-\infty}^{\infty} \frac{s(\tau)}{t - \tau} d\tau \quad (3.1)$$

The definition of analytic signal is

$$s(t) = A(t)\exp(i\varphi_i(t)) \quad (3.2)$$

where  $A(t)$  and  $\varphi(t)$  are the instantaneous amplitude and phase, respectively. To extract the instantaneous phase from the signal  $s(t)$  the following definition is used

$$\phi(t) = \arctan \frac{\Im H[s(t)]}{\Re H[s(t)]} \quad (3.3)$$

where  $\Im$  and  $\Re$  correspond to Imaginary and Real components, respectively. From the above equation we can see that HT can only give us a time average phase in a time window. Therefore, the time resolution is the main advantage of this technique.

Within the scope of the presented work, the measured azimuth angle of rotor  $i$  can be calculated by defining the  $t_p$  as the time when the propeller passes for the first time the  $x_i$ -axis at the desirable rotational speed, i.e. when it is rotating at 95% of its mean rotating speed, so the calibrated azimuth angle shall be:

$$\varphi_i(t) = \phi(t) - \phi(t_p) \quad (3.4)$$

Then, a calibrated magnetic encoder constructs, as the following:

$$S(t) = \sin(\varphi_i(t)) \quad (3.5)$$

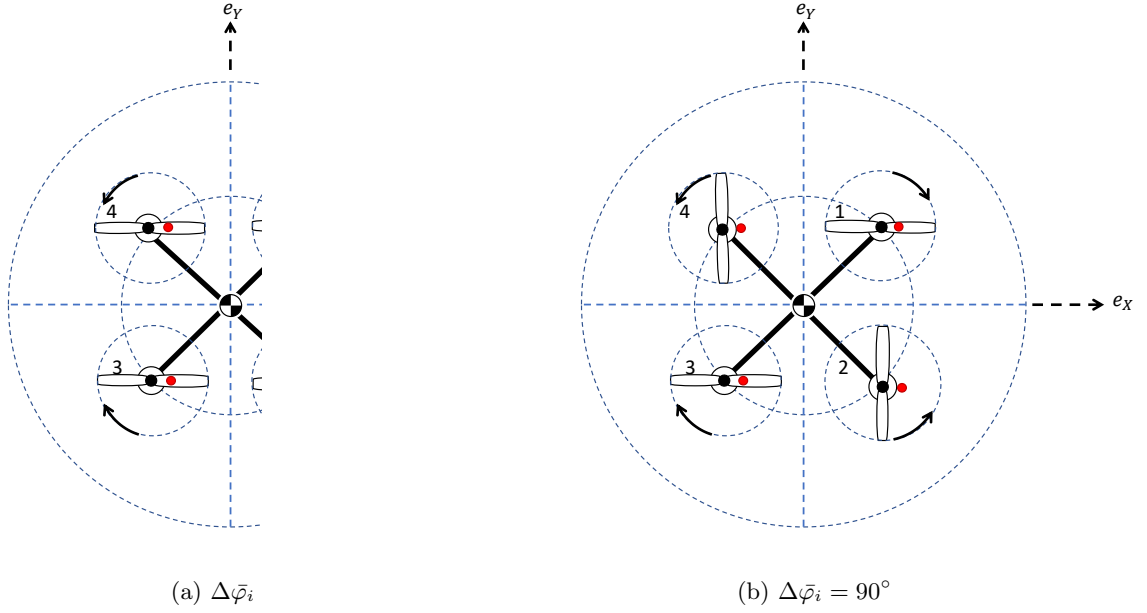


Figure 3.5: Definition of the synchronization of the four rotors in the experimental rig.

which is constructed for visualisation purposes.

To detect the instantaneous position of each propeller two step approach was implemented. In the first step, optic encoder was used to detect the position of the rotor with respect to the microphones; whereas, in the second step, magnetic encoder was used to measure the instantaneous phase. To obtain the instantaneous phase, Hilbert transform is performed on a low-pass digital filtered encoder signal in order to minimize disturbances due to the complexity of the sampling measurements. Letting motor  $M_1$  be the reference motor, the phase difference calculation becomes

$$\Delta\varphi_i = \varphi_i - \varphi_1 \quad (3.6)$$

then to visualize the implementation of the phase control, the subtraction between every relative phase to the reference rotor in shown in Table 3.1. For clarity, the following abbreviations are used to describe  $\Delta\bar{\varphi}_i$ .

$\Delta\bar{\varphi}_i = 0^\circ$	$\Delta\varphi_i = [0^\circ \ 0^\circ \ 0^\circ \ 0^\circ]$
$\Delta\bar{\varphi}_i = 90^\circ$	$\Delta\varphi_i = [0^\circ \ 90^\circ \ 0^\circ \ 90^\circ]$

Table 3.1: Definition of synchronization as shown in Figure 3.5

Figures (3.6a) and (3.6b) show application at  $\Delta\bar{\varphi}_i = 0^\circ$  and Figures (3.6c),(3.6d) show  $\Delta\bar{\varphi}_i = 90^\circ$  at  $3000RPM$ . The relative phase in both cases are oscillating at range of  $40^\circ$  as opposed to their steady-state command. The estimated signal which shown in (3.6b) and (3.6d) demonstrate how efficient the controller is. There is no visual differences between the relative signal at  $\Delta\bar{\varphi}_i = 0^\circ$ .

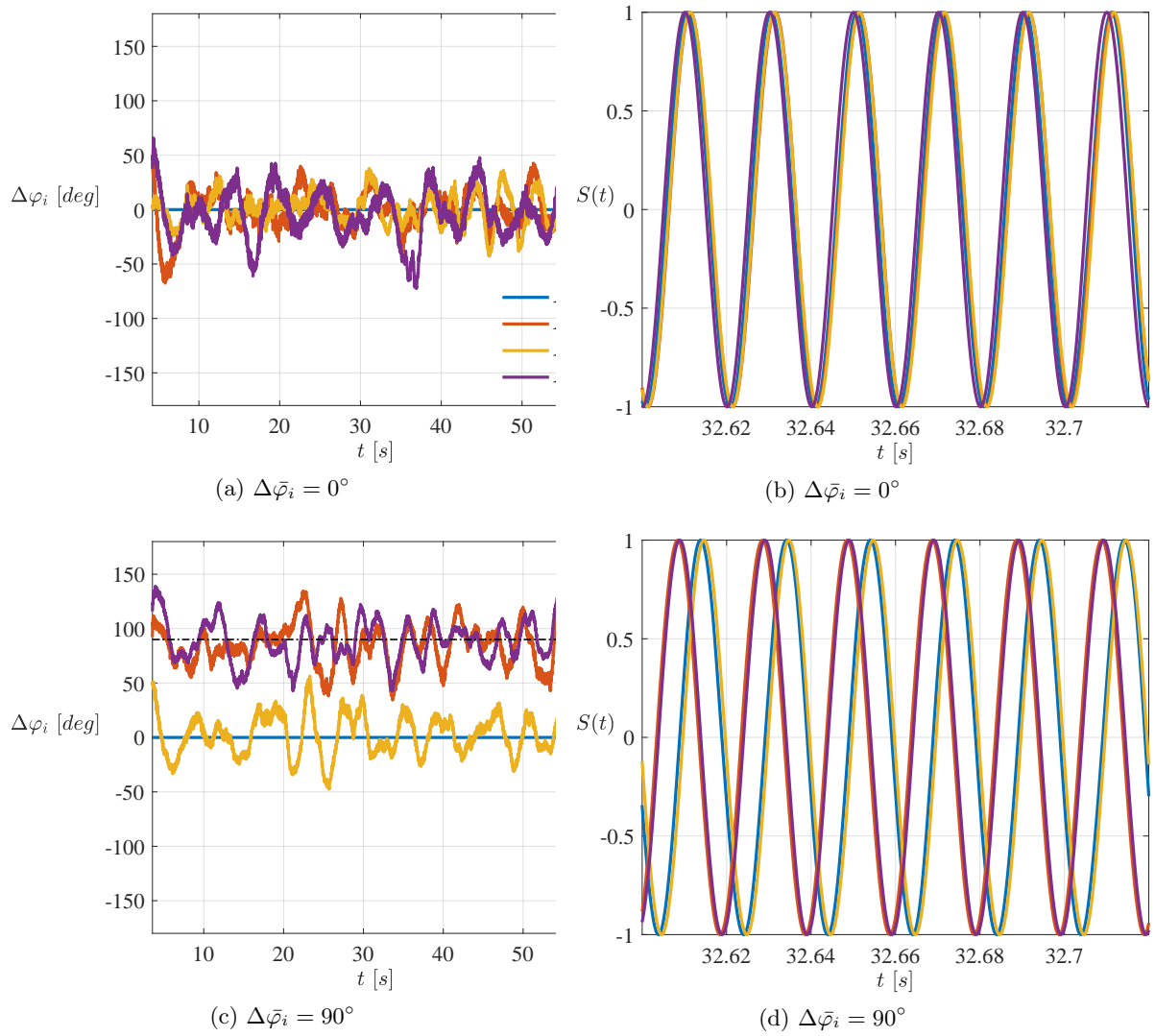


Figure 3.6: Illustration of phase control algorithm at 3000 RPM. Figures 3.6a and 3.6c show phase difference with respect to reference motor  $M_1$ , whereas Figures 3.6b and 3.6d show estimated signal.

### 3.2.2 Aerodynamic Performance

The thrust and torque that are exerted by the propeller are a function of its diameter and motor shaft rotational speed. According to momentum theory, the thrust generated by a propeller is proportional to the velocity squared. Propeller thrust  $C_T$  and torque  $C_Q$  coefficients, and figure of merit (FM) were obtained using the following definitions:

$$C_T = \frac{F_z}{\rho(\Omega/2\pi)^2 D^4} \quad (3.7)$$

$$C_Q = \frac{M_z}{\rho(\Omega/2\pi)^2 D^5} \quad (3.8)$$

and

$$FM = \frac{C_T^{3/2}}{\sqrt{2}C_P} \quad (3.9)$$

where  $\rho$  is the air density,  $D$  is the propeller diameter,  $\Omega$  is the motor shaft rotational velocity, and  $C_P = 2\pi C_Q$  [41].

The corresponding aerodynamic coefficients are shown in Figure 3.7. At hover conditions, the aerodynamic coefficients remain constant with the increase in motor shaft rotational speed, thus suggesting aerodynamic similarity. Furthermore, there is no significant difference between  $\Delta\bar{\varphi}_i = 0^\circ$ ,  $\Delta\bar{\varphi}_i = 90^\circ$  and without any phase control. This results can provide more insight about the main effect of synchronization on the mean loads acting on the rotors, which appears negligible compare to the acoustic reduction potential that this technology has to offer. However, while comparing this results with the mean loads of a single rotor, the difference is much more significant - up to 7% with respect to the single rotor, as shown in figure 3.7.

### 3.2.3 Acoustic signature

Acoustic signature of modern rotating machinery composed of broadband noise, distributed over a very wide spectrum, and a series of superimposed discrete tones at multiples of the blade passing frequency (BPF) and its harmonics, rising above the broadband noise discrete frequencies. With phase control, the main interest is attenuation of the tonal contribution.

The direction in which the sound pressure radiates is important in determining its significance. In general, the BPF and its harmonics dominate the tonal contribution, and noise level decreases as the order increases. In the case of a multi-rotor, the influence of higher order harmonics may be significant due to the aerodynamic and acoustic unsteady effect caused by wake interactions and unsteady blade motion. However, the most fundamental effect pertains to the lower-order

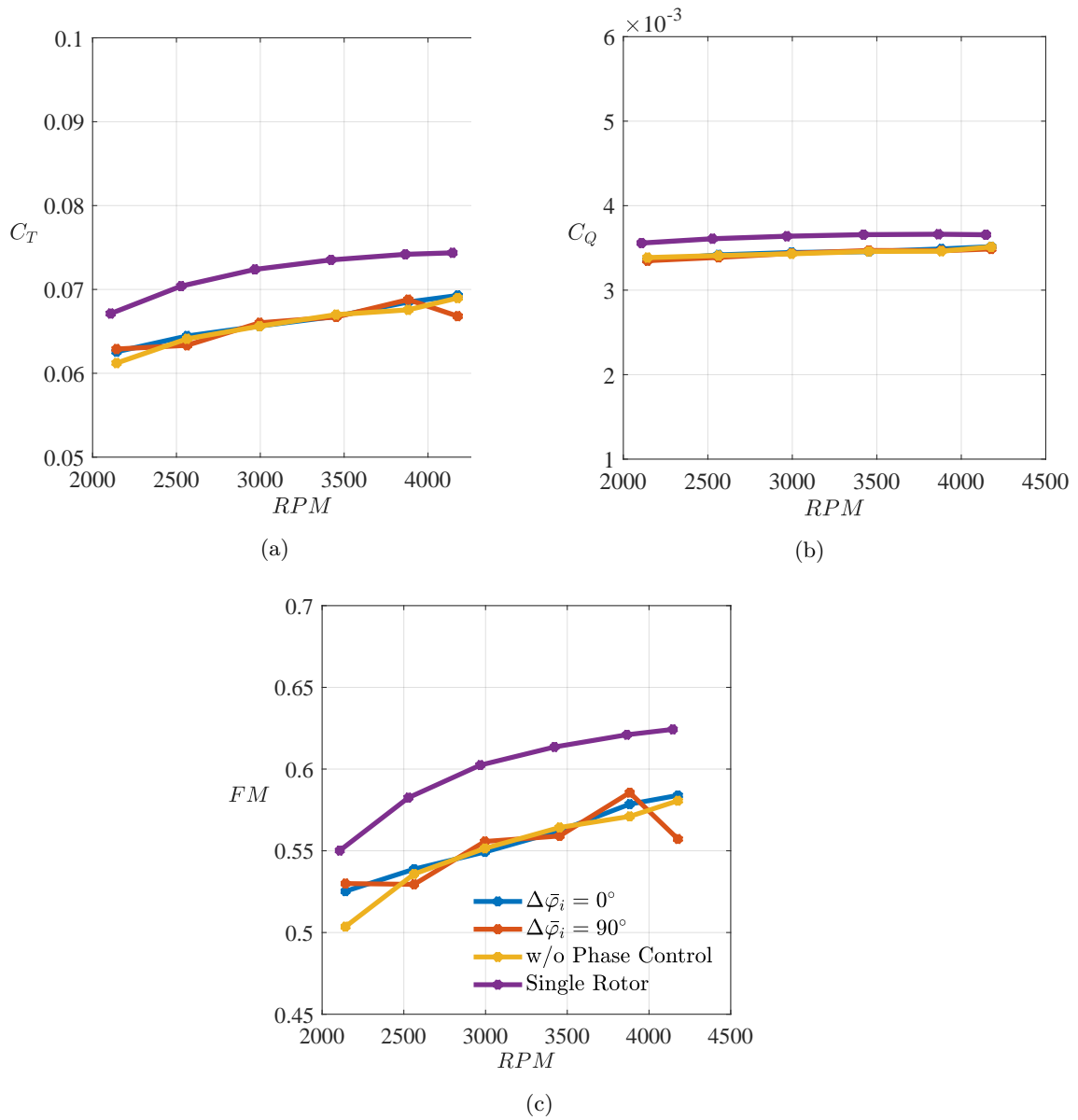


Figure 3.7: Comparison of thrust, (3.7a) and torque (3.7b) coefficients, and FM (3.7c) for the single propeller ( $M_1$ ) and four propellers ( $M_1 - M_4$ ) as a function of shaft rotational frequency, with and w/o phase control.

harmonics, since the first order harmonics dominate acoustic signature in the far-field (due to atmospheric absorption).

Figure 3.8 shows typical sound pressure level spectra at two observer locations and two motor shaft rotational speed. When the far-field noise spectra of the microphone observers is compared, the sound directivity of the tonal and broadband components is clearly apparent. For the low frequency range the  $\Delta\bar{\varphi}_i = 0^\circ$  and  $\Delta\bar{\varphi}_i = 90^\circ$  control produce different results, in comparison to propellers without phase synchronization. The  $\Delta\bar{\varphi}_i = 0^\circ$  produces up to 4 dB more compared to propellers without phase synchronization at the first BPF, suggesting this particular control method perhaps contributes to the constructive interference between the blade's wake or even the tip vortices. However, the  $\Delta\bar{\varphi}_i = 90^\circ$  control case produces up to 6 dB less in comparison to propellers without phase synchronization, suggesting this particular control perhaps contribute to the destructive interference between the blade's wake. When two neighboring rotors are passing by at  $\Delta\bar{\varphi}_i = 0^\circ$  configuration, their tips are at close proximity, in contrast to the  $\Delta\bar{\varphi}_i = 90^\circ$  configuration. As mentioned in previously published work [42, 43], rotor-to-rotor interaction can lead to larger pressure perturbation and ultimately to higher acoustic signature. At higher frequency range the differences are negligible, so it can be said that the broadband level is roughly the same.

Another way to interpret the measurements are via band sound pressure level (or *BSPL*). The tonal and broadband sound directivity can be better observed by integrating the contribution and plotting the *BSPL* as a function of the microphone observer position. The *BSPL* is estimated according to the following definition

$$BSPL = 10 \log_{10} \left( \frac{G_{pp}(f)}{p_{ref}^2} \right) \quad (3.10)$$

with

$$G_{pp}(f) = \int_{f_1}^{f_2} p^2(f) df \quad (3.11)$$

where  $f_1$  and  $f_2$  denote the lower and upper frequency limits within which the band sound pressure level was evaluated. The single sided one-dimensional spectrum  $G_{pp}$  is used to express the SPL. The sound pressure level is given in units of dB relative to the standard reference pressure of  $p_{ref} = 20 \mu\text{Pa}$ .

In the low frequency range, around the BPF, a range of  $\pm 15$  Hz is selected for the calculation of BSPL. To limit the effects of the motor self-noise on the interpretation of the acoustic measurements, and thus distinguish between motor noise and the propeller's contribution, it is important to choose an appropriate frequency band along which to perform the integration. When choosing the frequency band, special care needs to be taken to make sure that only relevant parts of the

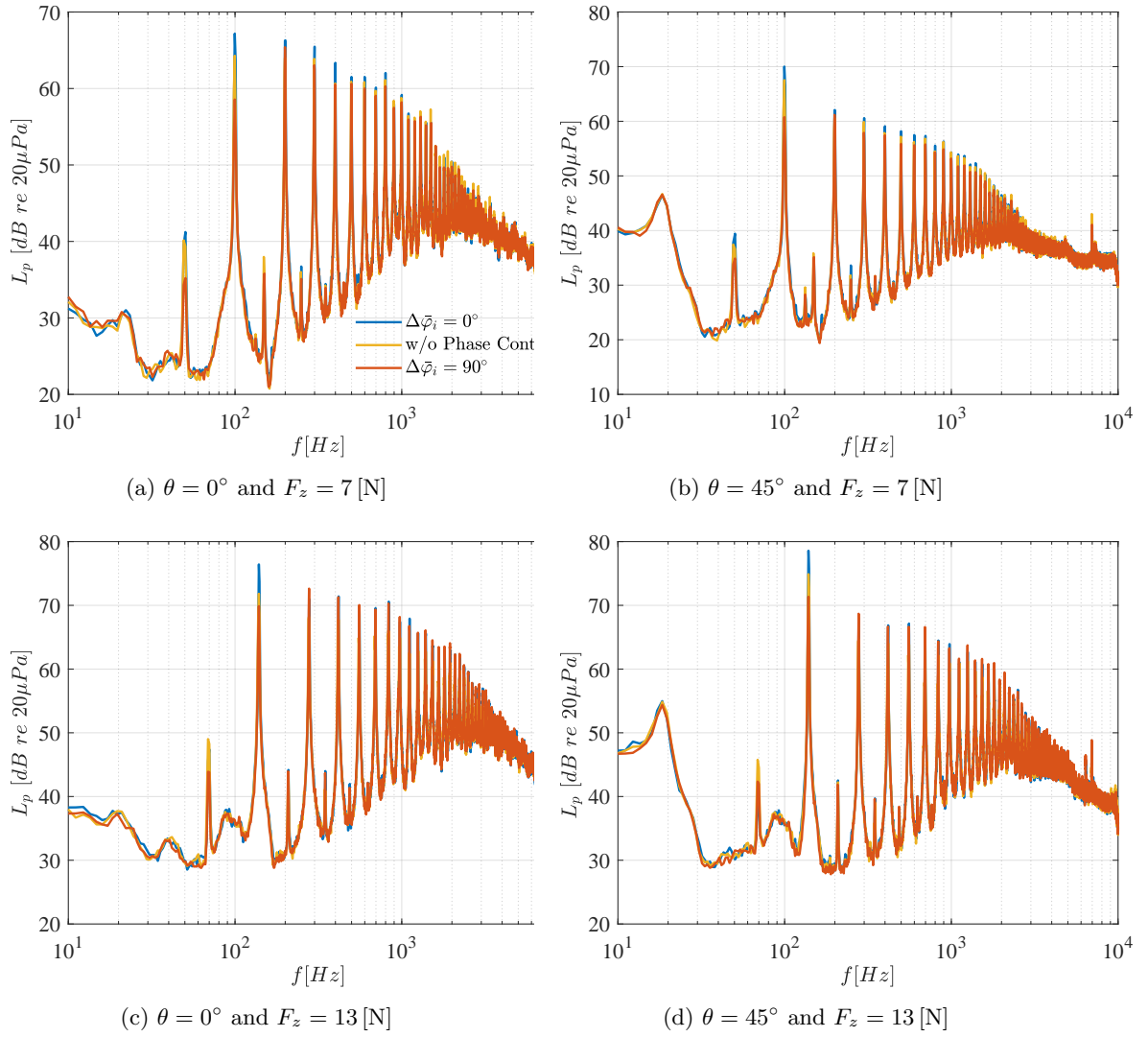


Figure 3.8: Comparison of one-dimensional far-field sound pressure level spectra with and without phase control.

spectra are selected. Therefore, the unloaded (with no propeller present) motor acoustic signature was measured separately, and then observed alongside the propeller to determine where it affected the propeller's frequency spectrum. Within the scope of the current study, broadband range was integrated between  $f_1 = 3$  kHz to  $f_2 = 10$  kHz, where the upper bound corresponds to half of the sampling rate.

Integrating the tonal and broadband contributions in the previously defined frequency bands, provides qualitative and quantitative comparison of these components' directivity. Figures 3.9 and 3.10 show the *BSPL* as a function of microphone observer position. Directivity plots highlight some of the results previously discussed through the propeller narrowband spectra (see figure 3.8). The shape of both tonal and broadband directivity patterns appear to be unaffected by the rotational speed. Both the tonal and broadband contributions exhibit dipole directivity with wide lobes. The broadband directivity shows maximum on the center of the system axis and minimum in the plane of rotation.

In the distributed-propeller configurations, not only the amplitude of the tone at the fundamental frequency is increased, but also the appear higher order harmonics. Moreover, when the propellers are installed in close proximity, the tonal amplitude at most BPF multiples is increased. This is attributed to the increase in unsteady loading, as discussed at section 3.2.2. Therefore, a comparison with single rotor was made. The goal is to compare the directivity of a single rotor acoustic signature to four-rotor configuration. This can be done while multiply the *BSPL* of a single rotor to model the magnitude of four rotors.

As shown in figures 3.9 and 3.10, it can be said in general that rotor-to-rotor interaction are increasing the tonal amplitude at BFP and the broadband, as compare to the model of single rotor. This tendency occurs in all rotational speed and in the majority of observer locations. Furthermore, at higher multiples of the BPF, there is higher variance between the two configuration, e.g. difference of almost 15 dB at the third harmonic. The contribution of modelling the acoustic signature of a single rotor is to validate the main hypothesis, which is acoustic interactions of small rotors can be reduce using phase control technology. The fact that the magnitude of acoustic signature at the BPF with phase control of type  $\bar{\Delta}\varphi = 90^\circ$  is much closer to the magnitude of the model of single rotor rather than acoustic signature four-rotor configuration without phase control is encouraging and can be used in the future as base of better active noise reduction.

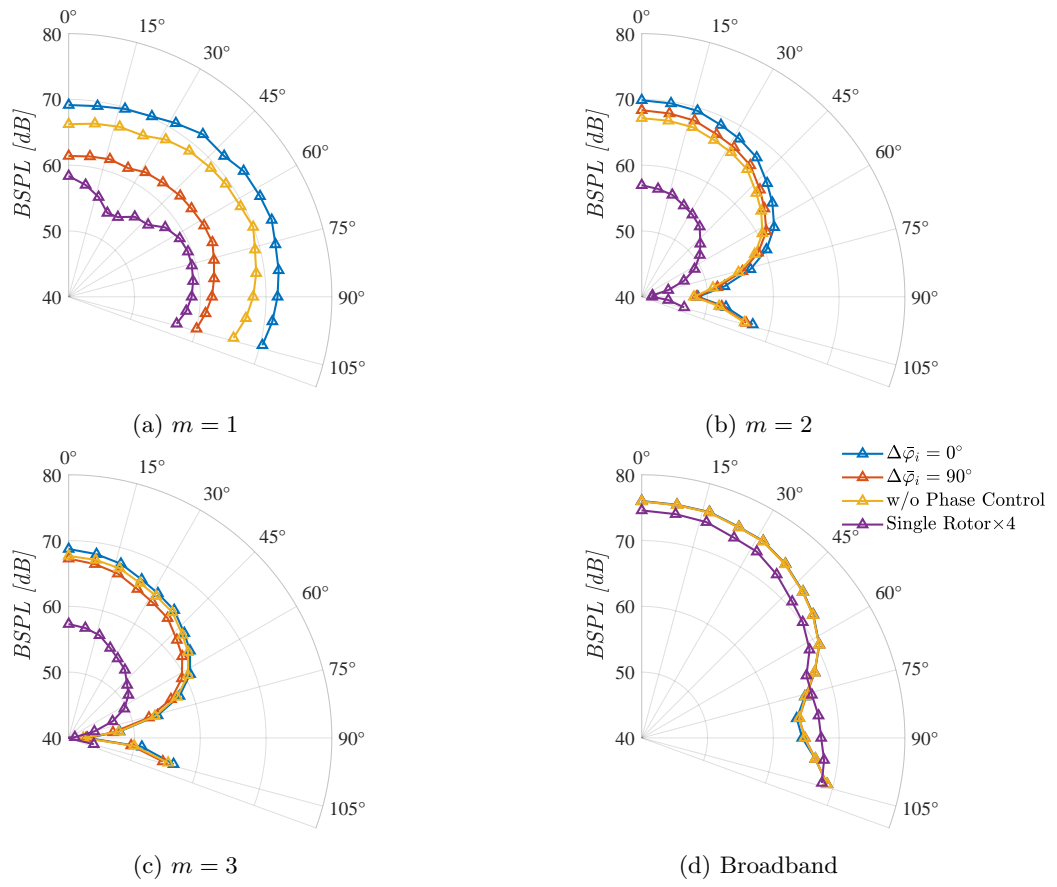


Figure 3.9: Directivity patterns of band sound pressure level at  $F_z = 7\text{ N}$ .

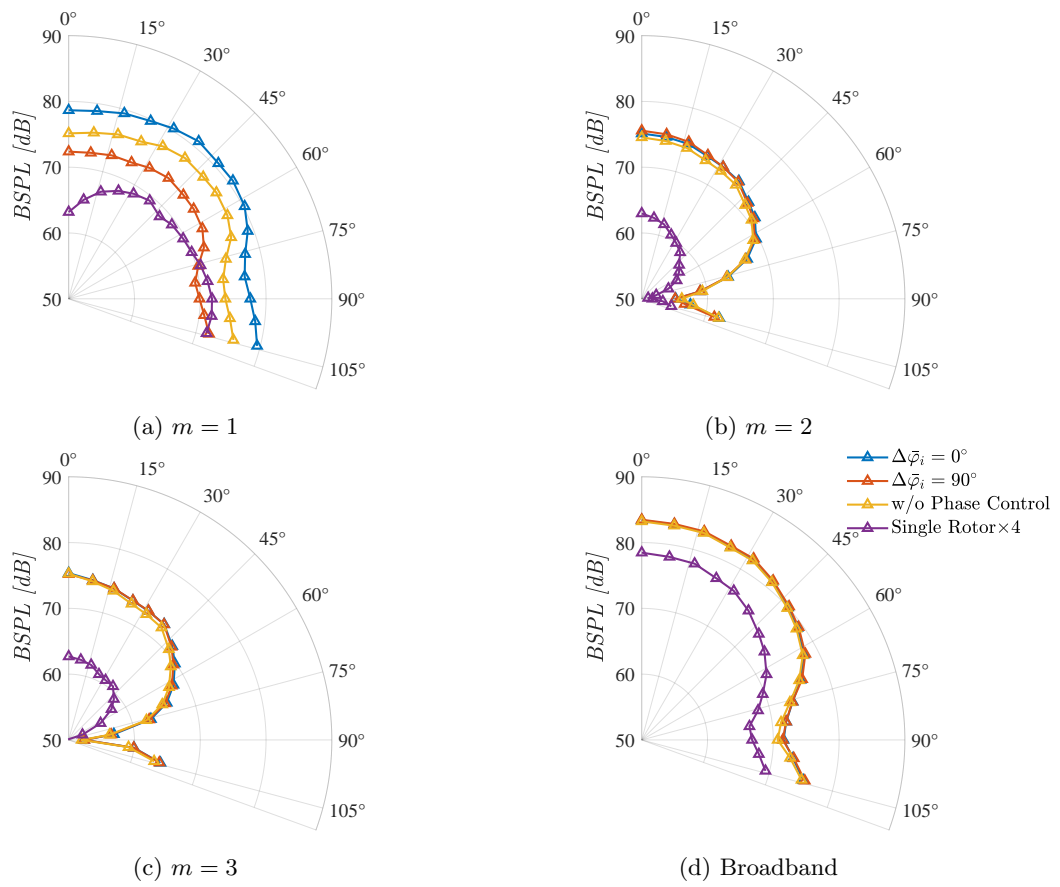


Figure 3.10: Directivity patterns of band sound pressure level at  $F_z = 13$  N.

### 3.3 Conclusion

Within the CAAI research project our main objective was to collect, process and archive noise signature data from single/multiple number of small-in-diameter propellers. The UASs are designed to operate within an urban environments, potentially exposing communities to significant levels of tonal and broadband noise. Current noise certification requirements, for fixed- and rotary-wing aircraft, may not adequately capture the noise effects of these vehicles. The only completed regulation that covers sUAS is 14 CFR part 107. The measurements in anechoic environment are intended to provide guidelines for community noise assessment.

The work commenced with performing literature review and acquisition of the necessary equipment. Following this step, the acoustic signature of a range of small-in-diameter isolated off-the-shelf APC Thin Electric propellers in static (hover) conditions has been investigated in the anechoic chamber in Dynamica Design. Above the cut-off frequency of the chamber, it is assumed that measurements conducted in anechoic chamber are performed in ideal environment. Furthermore, it is assumed that the acoustic measurements were conducted at the far-field, where the noise decay spherically from the source (the measured pressure amplitude from the propeller decays like  $1/r$ ). It is known that disturbances close to the propeller blade are dominated by evanescent pressure waves (so called pseudo-sound waves) that decay within the first few wavelengths from the source and do not propagate to the far-field. The spherical decay law for multi-drone measurements in the anechoic chamber was verified by Tinney and Sirohi [12].

During all the experimental work, acoustic and aerodynamic data were collected simultaneously. In processing of the data, the effect of shaft rotation speed and propeller diameter on the aerodynamically generated sound was studied. The discussion is separated into the tonal (deterministic) contribution at the BPF and the broadband contribution in the mid-high frequency range. Acoustic results show that the measured noise is a strong function of receiver angle. Both broadband and tonal components are a function of propeller diameter. The smaller-in-diameter propeller produced significantly stronger tonal and broadband noise contribution for a given level of thrust.

At the second stage (year II) focus was made to understanding the combined signature of four propellers in hover. A dedicated experimental rig was build to support four propellers. An algorithm was developed that allows to synchronize the rotational frequency and phase of all the propellers. Load-cell sensors were placed under the motors to allow measurement of aerodynamic forces and moments. During the second stage the focus was the role of synchronization in the generation of the acoustics signature, where the  $\varphi_i = [0\ 90\ 0\ 90]$  is the quieter configuration.

### 3.4 Future Directions

As a sound wave travels through the atmosphere it loses energy. The first and most important process is the geometric spreading, due to distance between the source and the observer. If one considers spherical wave spreading from a point source of uniform intensity, the sound pressure level at the observer varies inversely as the square of the distance from the source. This relationship is valid for non-point sources if the observer is in the far field. Expressed in terms of the logarithmic decibel scale, the sound pressure level falls by 6 dB for every doubling of distance from the source.

The other two processes, by which a sound wave loses energy, are functions of the atmosphere itself. The first mechanism arises through losses from heat conduction, radiation, viscosity, and diffusion. This is generally termed classical absorption and is proportional to the square of the sound frequency. The other process are associated with molecular relaxation in the air and, unlike classical absorption, is a function of humidity as well as frequency. Typically, this second effect is much more important in the audible range of frequencies, and classical absorption is generally neglected. The lower-frequency sound waves, comprising longer wavelengths, are less susceptible to atmospheric absorption.

As discussed previously, current regulations include the option to apply for a certificate of waiver, which allows for a UASs operation (under 55 pounds) to deviate from certain operating rules. However, these vehicles are nuisance and therefore an alternative noise metric should be applied to assess the noise and environmental impacts of these vehicles. Thus, recommendations for future work include continuing the development of the noise measurements procedures, expanding the database of UAS noise measurements, and working with other subject matter experts on the psychoacoustics. This can be achieved in the next phase of the ASSURE project.

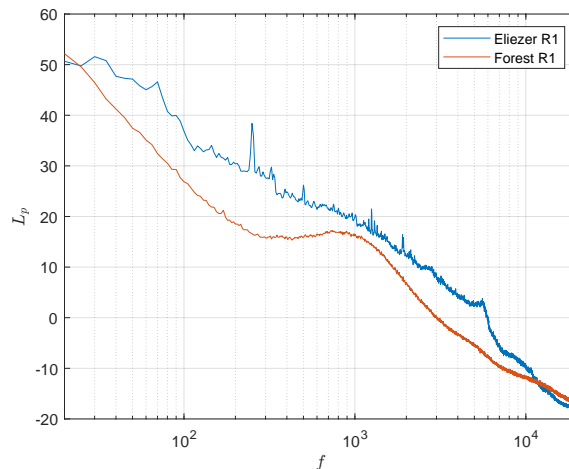


Figure 3.11: Measured background noise levels spectra at Haifa and forest environment.

Measurement of the background noise is important since the ability to detect acoustic signature is determined by the background noise levels. Figure 3.11 shows measured background spectrum at one of the neighborhoods at Haifa and forest environment, corresponding to the background noise level at urban and desert soundscape.

Furthermore, the perception of human hearing must be accounted for when planning flight with significant acoustic radiation. For example, human hearing is most sensitive to noise in the frequency range between 2 and 5 kHz, which means that sounds in this range are perceived as being louder than the same sound level at frequencies outside of this range [44]. The field of psychoacoustics has developed many factors that attempt to account for human perception, such as loudness and noisiness. Loudness accounts for frequency sensitivity and noisiness for fluctuations in amplitude in sound that are perceived as annoying by a human.

These considerations are included in existing noise metrics such as EPNL and SEL but the implementation may need to be modified for these new class of vehicles. Sound quality metrics (SQMs) are associated with different noise characteristics, such as the frequency content (high or low frequency), the prominence of tones, and the fast or slow loudness fluctuations. The five SQMs loudness, roughness, sharpness, tonality, and fluctuation strength provide a detailed characterization of a sound; and they can be combined toward an overarching psychoacoustic metric. These metrics then provide a single value similar to the EPNL and LA maximum, allowing us to compare the annoyance of different sounds. Recent work considered the psychoacoustic metrics as a more accurate method to determine the annoyance perceived by the human ear than EPNL [45].

Another approach that determines the ability of a human to detect specific sounds in a noisy background is by using a computational model of the auditory system. The model's input is an acoustic signal that includes the targeted sound embedded in a given background noise and its output is the probability of a human listener to detect the targeted sound. The model includes the following steps: performance in a threshold task. A task in which the listener indicates the minimal level of the targeted sound he can detect in a given background noise. This framework was developed by Siebert [46], followed by Heinz et al [47] and Furst [48]. The computational model is stimulated by an acoustic stimulus and its output is the threshold in quiet.

# Appendix A

## Aerodynamic Model

BEMT is a low fidelity model that requires limited computational resources, compared to the high-fidelity computational fluid dynamic (CFD). The efficiency comes at the price of having to know, for the total number of blade sections, the two dimensional airfoil parameters, namely, lift  $C_l(\alpha, M, Re)$  and drag  $C_d(\alpha, M, Re)$  aerodynamic coefficients over a wide range of **angles of attack**  $\alpha$ , **Mach numbers**  $M = \frac{U}{c_0}$ , where  $U$  is the velocity magnitude and  $c_0$  is the speed of sound, and **Reynolds number**  $Re = \frac{\rho UL}{\mu}$  where  $\rho$  is the air density,  $\mu$  is kinematic viscosity and  $L$  is a characteristic length scale. Evaluation of low fidelity XFOIL and BEMT methods for the aerodynamic performance of a UAV propellers is common practice [49, 50].

The development of theories embodied in BEMT models goes back to the pioneering works of Rankine [51] and Froude [52]. These studies were the first to propose the formation of an actuator disk of negligible thickness. The idea of the blade element was proposed by Drzewiecki [53], and latter enhanced by Prandtl. The hybrid theory, which merges the actuator disk with the blade element, emerged in 1926 due to Glauert [54], called BEMT. Subsequently, improvements in the BEMT were proposed by Theodorsen [55], Larrabee [56], as well as Adkins and Liebeck [57]. Nowadays, this theory is still widely used for the aerodynamic study of rotating systems, such as propellers and wind turbines.

BEMT is an extensively used technique for calculation of propeller aerodynamic performance. With this method, the airfoil data base needs to be as accurate as possible. At the same time, Computational Fluid Dynamics (CFD) is becoming increasingly popular in the design and optimization . For fixed and rotary wing applications, the airfoil lift over drag coefficient is the dominant airfoil performance parameter. Selecting a suitable computational tool is crucial for the successful design and optimization of this ratio. Potential flow theory is commonly used to evaluate the aerodynamic performance of airfoils, airplanes, wind blades, etc. when speed is preferred over accuracy.

Drela [58] presented an analysis and design system for low Reynolds number airfoils called XFOIL. In this system, the potential flow is coupled with viscous models, allowing it to capture viscous effects while maintaining the computational advantages of the potential flow. The boundary layer and transition equations are simultaneously solved with the inviscid flow-field, thus, suitable for rapid analysis of low Reynolds number airfoils with separation bubbles. Besides, the grid density must be sufficient to define the surface of the geometry, since XFOIL's formulation is a simple linear-vorticity stream function panel method and the accuracy of results depends on the number of panels.

The model radially discretize the propeller blade geometry into spanwise annuals. Each blade element can be considered as a rotating lifting surface. For simplicity, it is assumed that the flow is two-dimensional. Using this assumption, each element is considered independent. The airfoil is positioned at a radial pitch angle  $\theta$  with respect to the plane of rotation, and immersed in a uniform flow given by the velocity magnitude  $U$ , and the induced angle of attack  $\phi$ , thus yielding the local effective angle of attack

$$\alpha = \theta - \phi. \quad (\text{A.1})$$

While the effective velocity defines as:

$$U = \sqrt{(U_a + W_a)^2 + (U_r - W_r)^2} \quad (\text{A.2})$$

where  $W_a$  and  $W_r$  are the axial and rotational induced velocity,  $U_a$  is the free-stream velocity and  $U_r = \omega r$ . Note that in case of a rotors  $U_a = 0$ , but for the completeness of the equations it has been assumed that  $U_a \neq 0$ . The blade element relative velocity and respective inflow angle are evaluated with the axial and rotational velocity components. By performing iterations the effective angle of attack can be found.

### A.0.1 Blade Element

According to Adkins [59] and Gur [60], the sectional thrust  $T$  per unit radius acting on the blade, can be expressed as a function of lift  $L$  and drag  $D$  per unit length, as describes in the figure below

$$\frac{dT^{BE}}{dr} = N_b(dL \cos \phi - dD \sin \phi) \quad (\text{A.3})$$

Where  $BE$  stands for Blade-Element and  $N_b$  is the number of blades. By similar argument, the torque per unit radius due to circumferential forces is given by applying a force balance to the

blade element in rotational directions

$$\frac{dQ^{BE}}{dr} = N_b r (dL \sin \phi + dD \cos \phi) \quad (\text{A.4})$$

And from figure A.1,  $\phi$  define as:

$$\phi = \tan^{-1} \frac{U_a + W_a}{U_r - W_r} \quad (\text{A.5})$$

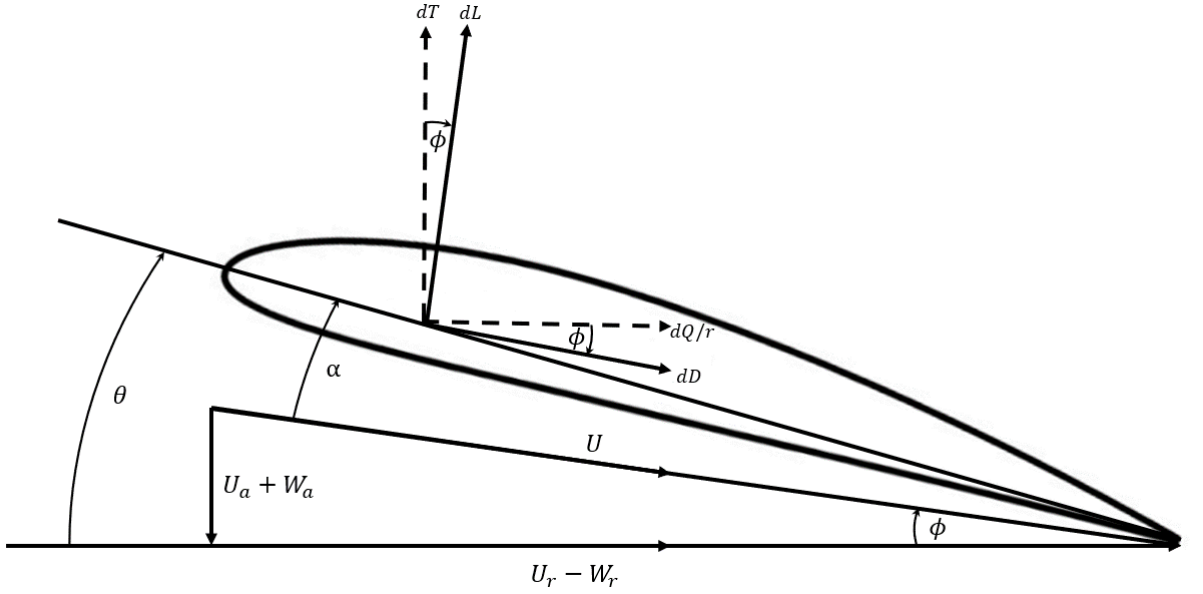


Figure A.1: Cross-section of a blade-element of a propeller at hover flight at radial station with sectional forces and velocities.

The contribution of each blade-element to the thrust and torque can be calculated using the appropriate transformation of the cross-sectional lift and drag forces. The main assumption is that there is no interactions between the elements.

## A.0.2 Momentum Theory

According to the momentum theory, the propeller is replaced by an actuator disk. The derivation of the governing equation of momentum theory can be found in [59]. The momentum equations are

$$\frac{dT^M}{dr} = 4\pi r \rho W_a (U_a + W_a) \quad (\text{A.6})$$

$$\frac{dQ^M}{dr} = 4\pi r^2 \rho W_r (U_a + W_a) \quad (\text{A.7})$$

Where  $M$  stands for momentum theory.

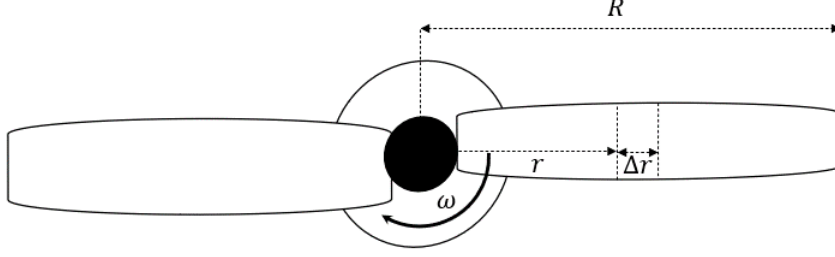


Figure A.2: Blade radial coordinates

### A.0.3 Derivation of BEMT

Utilizing and combining the blade element and momentum equations, the following equilibrium is defined:

$$\frac{dT^{BE}}{dr} \equiv \frac{dT^M}{dr} \quad (\text{A.8})$$

$$\frac{dQ^{BE}}{dr} \equiv \frac{dQ^M}{dr} \quad (\text{A.9})$$

The four unknowns of the mathematical problem are  $\frac{dT}{dr}$ ,  $\frac{dQ}{dr}$ ,  $W_a$ ,  $W_r$ . In order to get closed mathematical problem, it is essential to define two explicit equations to the induced velocities. It is suggested to utilizing a iterative set of problem to derive set of explicit equations. For convenience, the equations shall be normalized by using the following definitions:

1. Normalized radial section

$$\bar{r} = \frac{r}{R} \rightarrow d\bar{r} = \frac{1}{R} dr \quad (\text{A.10})$$

2. Lift and drag coefficients

$$\begin{aligned} C_L &= \frac{L}{\frac{1}{2}\rho U^2 c} \\ C_D &= \frac{D}{\frac{1}{2}\rho U^2 c} \end{aligned} \quad (\text{A.11})$$

3. Thrust and torque coefficients

$$\begin{aligned} C_T &= \frac{T}{\rho n^2 D^4} \\ C_Q &= \frac{Q}{\rho n^2 D^5} \end{aligned} \quad (\text{A.12})$$

4. Velocity ratio

$$\begin{aligned}\lambda &= \frac{U}{\omega R} \\ \lambda_a &= \frac{U_a}{\omega R}\end{aligned}\tag{A.13}$$

5. Blade's solidity

$$\sigma = \frac{N_b c}{2\pi R}\tag{A.14}$$

6. Axial and rotational velocity ratio

$$a_0 = \frac{W_a}{\omega R}\tag{A.15}$$

$$a_r = \frac{W_r}{\omega R}\tag{A.16}$$

The normalization of the blade-element-thrust goes as follows:

$$\begin{aligned}\frac{dC_T^{BE}}{d\bar{r}} &= \frac{1}{\rho n^2 D^4} \frac{d\Gamma}{d\bar{r}} = \frac{R}{\rho n^2 D^4} \frac{d\Gamma}{dr} \\ &= \frac{N_b \frac{1}{2} \rho U^2 c (C_l \cos \phi - C_D \sin \phi) R}{\rho n^2 2 R D^3} \\ &= \frac{\frac{1}{2} U^2 c (C_l \cos \phi - C_D \sin \phi)}{2 \frac{\omega^2}{4\pi^2} 8 R^3} \\ &= \frac{\pi^3 \frac{N_b c}{2\pi R} \frac{U^2}{\omega^2 R^2} (C_l \cos \phi - C_D \sin \phi)}{4} \\ &= \frac{1}{4} \pi^3 \lambda^2 \sigma (C_l \cos \phi - C_D \sin \phi)\end{aligned}\tag{A.17}$$

On the same way we can normalize the remaining of the equations to derive:

$$\begin{aligned}\frac{dC_Q^{BE}}{d\bar{r}} &= \frac{1}{\rho n^2 D^5} \frac{dQ}{d\bar{r}} = \frac{R}{\rho n^2 D^5} \frac{dQ}{dr} = \\ &= \frac{N_b r \frac{1}{2} \rho U^2 c (C_l \sin \phi + C_D \cos \phi) R}{\rho n^2 2 R D^4} \\ &= \frac{\frac{1}{2} U^2 r c (C_l \sin \phi + C_D \cos \phi)}{2 \frac{\omega^2}{4\pi^2} 16 R^4} \\ &= \frac{\pi^3 \frac{r}{R} \frac{N_b c}{2\pi R} \frac{U^2}{\omega^2 R^2} (C_l \sin \phi + C_D \cos \phi)}{8} \\ &= \frac{1}{8} \pi^3 \lambda^2 \bar{r} \sigma (C_l \sin \phi + C_D \cos \phi)\end{aligned}\tag{A.18}$$

$$\begin{aligned}
\frac{dC_T^M}{d\bar{r}} &= \frac{1}{\rho n^2 D^4} \frac{dT^M}{d\bar{r}} = \frac{R}{\rho n^2 D^4} \frac{dT^M}{dr} \\
&= \frac{4\pi\rho RrW_a(U_a + W_a)}{\rho n^2 2RD^3} \\
&= \frac{4\pi rW_a(U_a + W_a)}{16R^3 \frac{\omega^2}{4\pi^3}} \\
&= \pi^3 \frac{r}{R} \frac{W_a(U_a + W_a)}{\omega^2 R^2} \\
&= \pi^3 \bar{r} a_0 (\lambda_a + a_0)
\end{aligned} \tag{A.19}$$

$$\begin{aligned}
\frac{dC_Q^M}{d\bar{r}} &= \frac{1}{\rho n^2 D^5} \frac{dQ^M}{d\bar{r}} = \frac{R}{\rho n^2 D^5} \frac{dQ^M}{dr} \\
&= \frac{4\pi\rho Rr^2W_r(U_a + W_a)}{\rho n^2 2RD^4} \\
&= \frac{4\pi r^2W_r(U_a + W_a)}{32R^4 \frac{\omega^2}{4\pi^3}} \\
&= \pi^3 \frac{r^2}{R^2} \frac{W_r(U_a + W_a)}{\omega^2 R^2} \\
&= \frac{1}{2} \pi^3 \bar{r}^2 a_r (\lambda_a + a_0)
\end{aligned} \tag{A.20}$$

The non-dimensional momentum equations can be arranged to define two explicit equations to the induced velocities:

$$a_0 = -\frac{1}{2}\lambda_a + \frac{1}{2}\sqrt{\lambda_a^2 + \frac{4}{\pi^3\bar{r}} \frac{dC_T}{d\bar{r}}} \tag{A.21}$$

$$a_r = \frac{2}{\pi^3\bar{r}^2(\lambda_a + a_0)} \frac{dC_Q}{d\bar{r}} \tag{A.22}$$

The iterative algorithm is defined in the "Convergence Algorithm" section. For more information regards the convergence method, the reader Referred to §A.0.6.

After convergence, the total thrust and torque defined by

$$\begin{aligned}
\frac{dT}{dr} &= \frac{dC_T}{Rd\bar{r}} \rho n^2 D^4 \\
T &= \int_{R_{hub}}^R \frac{dT}{dr} dr
\end{aligned} \tag{A.23}$$

and

$$\begin{aligned}
\frac{dQ}{dr} &= \frac{dC_Q}{Rd\bar{r}} \rho n^2 D^5 \\
Q &= \int_{R_{hub}}^R \frac{dQ}{dr} dr
\end{aligned} \tag{A.24}$$

### A.0.4 Tip Correction Function

As mention before, by using BEMT it is assumed that there is no interactions between the blade elements, as that is no tip interactions. As known from basic aerodynamics, tip interactions crates reduction of the lift forces near the tip, duo to pressure equalization. The formulation developed by Prandtl is calculated using

$$F(r) = \frac{2}{\pi} \cos^{-1} \left( e^{-f} \right) \quad (\text{A.25})$$

where

$$f = \frac{N_b(R-r)}{2r \sin \phi}. \quad (\text{A.26})$$

$F$  varies from 1 near the hub and approaching 0 near the blade's tip. The tip correction is a function of the flow angle as well, so it can not be drawn for general case. The derivation of the tip correction function can be found in [61].

To take into account this effect, Prandtl [59] multiply the momentum equations with the tip correction function:

$$\begin{aligned} \frac{dT_{tip\ corr}^M}{dr} &= F(r) \times \frac{dT^M}{dr} \\ \frac{dQ_{tip\ corr}^M}{dr} &= F(r) \times \frac{dQ^M}{dr} \end{aligned} \quad (\text{A.27})$$

The explicit induced velocities equations are equal to

$$a_0 = \frac{1}{2}\lambda_a + \frac{1}{2}\sqrt{\lambda_a + \frac{4}{F\pi^3\bar{r}}\frac{dC_T}{d\bar{r}}} \quad (\text{A.28})$$

$$a_r = \frac{2}{F\pi^3\bar{r}^2(\lambda_a + a_0)}\frac{dC_Q}{d\bar{r}} \quad (\text{A.29})$$

### A.0.5 Post stall Aerodynamic Database

Airfoil lift and moment coefficients in the high Reynolds and low angle of attack regime is readily available from multitude of sources, for instance Abbott and von Doenhoff [62], and University of Illinois at Urbana Champaign database [63, 64, 65]. For many applications, data in this linear regime is sufficient. However, post-stall flight dynamics of fixed wing vehicle require data to extend beyond aerodynamic stall. Efforts have been made in propeller aerodynamics communities to extend airfoil databases into the high angle-of-attack, i.e. post-stall regime. This led to researchers proposing empirical models based on flat plate theory [66], semi-empirical methods [67] [68] [69], and aerodynamic databases [70] [71]. This semi-empirical models are important since the post stall lift and drag prediction with XFOIL are still not accurate with the present method as this type of

a computational method for prediction flow around airfoils becomes inaccurate as the boundary layer becomes too thick when separation commence. Furthermore, the empirical models developed from experiment require that both the maximum  $C_l$  and the corresponding  $\alpha_s$ , at which this lift coefficient occurs is known reliably before theoretical flat plate model may be fitted to extend the data well into post-stall regime. The flat plate extension will be combined from angle of attack higher then  $\alpha_s$  to guarantee continuity with pre-stall data. The lift and drag coefficients shall be equal to

$$C_L^{Post-Stall} = A_1 \sin 2\alpha + A_2 \frac{\cos^2 \alpha}{\sin \alpha} \quad (\text{A.30})$$

$$C_D^{Post-Stall} = B_1 \sin^2 \alpha + B_2 \cos \alpha \quad (\text{A.31})$$

where

$$A_1 = \frac{B_1}{2} \quad (\text{A.32})$$

$$B_1 = C_{D_{max}} \quad (\text{A.33})$$

according to [66]

$$C_{D_{max}} \cong 1.11 + 0.018AR \quad (\text{A.34})$$

therefore

$$A_1 = \frac{C_{D_{max}}}{2} \quad (\text{A.35})$$

and

$$A_2 = (C_{L_{max}} - B_2 \sin \alpha_s \cos \alpha_s) \frac{\sin \alpha_s}{\cos^2 \alpha_s} \quad (\text{A.36})$$

$$B_2 = C_{D_s} - \frac{C_{D_{max}} \sin^2 \alpha_s}{\cos \alpha_s} \quad (\text{A.37})$$

## A.0.6 Convergence Algorithm

As explained above, BEMT is an iterative method for estimating the thrust and the torque for a given rotor and operating conditions. The convergence method is controlled by constant threshold,  $\varepsilon > 0$ , which is defined by the user. Normally,  $\varepsilon = 10^{-3}$  ensures convergence of the physical output. The user must input the rotor geometry i.e.  $R, \theta(r), c(r), N_b$  and the operating condition - the RPM. The user must also input the aerodynamic database that was prepared in advance

for the aerodynamic profiles of the rotor. To initialize the iterative solution, an initial guess is made to the normalized induced velocities  $a_0, a_r$ . to begin the convergence sequence, their value must be bigger than  $\varepsilon$ . In every iteration, the aerodynamic conditions at every section i.e.  $Re(r), \alpha(r), M(r), C_l(r), C_D(r)$  is modified using the updated values of  $a_0, a_r$ . Then, the coefficients of thrust and torque are calculating using ( A.17) and ( A.18) as well. to update the new value of  $a_0, a_r$ , the convergence sequence are utilizing (A.28) and (A.29). This sequence continue until

$$|a_{0_{new}}(r) - a_{0_{curr}}(r)| < \varepsilon \ \&\& \ |a_{r_{new}}(r) - a_{r_{curr}}(r)| < \varepsilon \quad (\text{A.38})$$

The convergence algorithm is described here as follows:

---

**Algorithm 1** Blade-Element Momentum Theory Code

---

- 1: **Input:**  $R, \theta(r), c(r), RPM, N_b, Aerodynamic\ database, \varepsilon > 0$
  - 2: **Initial Guess:**  $a_0, a_r$
  - 3: **while**  $|a_{0_{new}} - a_{0_{curr}}| > \varepsilon \ \&\& \ |a_{r_{new}} - a_{r_{curr}}| > \varepsilon$  **do**
  - 4:      $a_{0_{curr}}(r), a_{r_{curr}}(r), RPM \rightarrow U(r)$
  - 5:      $U(r), R, RPM \rightarrow \phi(r), \alpha(r), Re(r), \lambda(r), \sigma$
  - 6:      $\alpha(r), Re(r) \rightarrow C_L(r), C_D(r)$
  - 7:      $C_L(r), C_D(r), \phi(r), N_b, \lambda(r), \sigma \rightarrow \frac{dC_T^{BE}}{d\bar{r}}(r), \frac{dC_Q^{BE}}{d\bar{r}}(r)$
  - 8:      $\frac{dC_T^{BE}}{d\bar{r}}(r), \frac{dC_Q^{BE}}{d\bar{r}}(r), \lambda(r), \sigma \rightarrow a_{0_{new}}(r), a_{r_{new}}(r)$
  - 9: **end while**
  - 10: **Multiply by Normalized Value:**  $\frac{dT}{dr} = \frac{dC_T}{d\bar{r}} \frac{\rho n^2 D^4}{R}, \frac{dQ}{dr} = \frac{dC_Q}{d\bar{r}} \frac{\rho n^2 D^5}{R}$
  - 11: **Global Output:**  $T = \int_0^R \frac{dT}{dr} dr, Q = \int_0^R \frac{dQ}{dr} dr$
  - 12: **Spanwise Output:**  $\frac{dT}{dr}, \frac{dQ}{dr}, \alpha(r), C_L(r), C_D(r), Re(r)$
- 

### A.0.7 XFOIL

XFOIL [58] is low fidelity model for the analysis of flow around airfoils. The model combines a potential flow panel method and an integral boundary layer formulation. The XFOIL code was developed to rapidly predict the airfoil performance at low Reynolds numbers and its convergence is achieved through the iteration between the outer and inner flow solutions on the boundary layer displacement thickness. Thus, the code calculates the viscous pressure distribution and captures the influence of limited trailing edge separation and laminar separation bubbles. For external flow solver airfoils and wings in wind tunnels, the main factor influencing the critical  $N_{cr}$  is the free-stream turbulence level of the test section. The XFOIL uses an approximate  $e^N$  envelope method to calculate transition.

As it is well documented, the behaviour of airfoils is strongly dependent on Reynolds numbers, particularly at the lower end ( $Re_c < 10^6$ ). For instance, airfoil drag in incompressible flow is constituted of shear related skin friction drag and pressure drag. Pressure drag component is

caused, at its most fundamental level, by a fore and aft imbalance in the net integrated streamwise pressure distribution, which is primarily caused by separation (open or closed, e.g., bubbles), or to a lesser extent by boundary-layer displacement thickness effects. The skin friction drag component in general shows the greatest sensitivity to Reynolds number, increasing significantly as  $Re_c$  drops.

The approximate  $e^N$  transition model of Smith and Gamberoni [72] and van Ingen [73] is based on linear stability theory. The method assumes that transition occurs when the maximum amplification ratio of any boundary-layer instability reaches a specified ratio,  $N_c$  along a predetermined integration path. The transition model used to emulate the changes in roughness and turbulent intensity level. While this ratio was originally taken to be  $e^9$  for typical aerodynamic configurations in low-turbulence environments, the model has been extended to account for varying free-stream turbulence levels [74]. With this method the code tracks only the most amplified frequency at a given point on the airfoil, downstream from the point of instability to obtain the amplitude of that disturbance. Transition is assumed when this integrated amplitude reaches an empirically determined value. The appropriate  $N_{cr}$  to use into XFOIL calculations, can be calculated by empirical correlation [74], as presented by van Ingen [73]

$$N_{cr} = -8.43 - 2.4 \ln \left( \frac{\tau}{100} \right) \quad (\text{A.39})$$

where  $Tu$  represents the absolute turbulence intensity and  $\tau$  is the correction.

$$\tau = 2.5 \tanh \left( \frac{Tu(\%)}{2.5} \right) \quad (\text{A.40})$$

Lower value of  $N_{cr}$  indicates on higher turbulence level. For example, 0.1% turbulence level indicate on  $N_{cr} = 8$ , compare to 0.5% turbulence level that yeilds  $N_{cr} = 4$ .

## Appendix B

# Aeroacoustic Model

Analytic modeling of a single propeller noise is based on the acoustic analogy that relies on a two-step approach. As a first step, the aerodynamic forces and moments are specified. Their sound radiation can be used in a second step. The sound field due to steady loads can be described with a series of discrete tones at frequencies that are multiples of the blade passing frequency (BPF). Both in quality and quantity, the sound predicted by this theory is in agreement with the experimental evidence of the far-field sound produced at high tip Mach number flows [75], since rotational noise is dominated by steady forces [22].

However, at low tip speeds, the propeller often operates in highly unsteady environment, which results in unsteady loads, and the corresponding blade loading harmonics. This high frequency harmonics rotate at multiples of BPF. Since propeller blades are thin, thickness noise is often negligible. Similarly, the quadrupole noise source is neglected, since the Mach number is relatively low. Consequently, only the dipole term is kept in prediction of higher order rotational noise. Lowson [76, 5] obtained a solution for the free-field radiation from point sources. The complex discrete rotor noise spectra can be analyzed into a set of simple blade-loading harmonics (BLH) radiations. The study of a propeller noise is then reduced to that of studying the individual properties of BLH radiation.

The sound pressure radiated by a point fluctuating force is

$$p(\mathbf{r}, t) = \left[ \frac{(x_i - y_i)}{(1 - M_r)c_0 r} \frac{\partial}{\partial t} \left( \frac{F_i}{4\pi r(1 - M_r)} \right) \right] \quad (\text{B.1})$$

where  $F_i$  is the point force acting at the source position,  $x_i$  in the  $i$ -th direction and  $M_r$  is the Mach number directed towards the observer at  $\mathbf{r}$ . The term at the square brackets should be evaluated at the retarded time  $\tau = t - r/c_0$ . This equation can be used to find expression for the sound from

a point force in arbitrary harmonic motion. Then, defining the complex magnitude of the  $n$ -th sound harmonic in the usual manner gives

$$c_n = a_n + ib_n = \frac{\omega}{\pi} \int_0^{2\pi/\omega} \left[ \frac{x_i - y_i}{(1 - M_r)c_0 r} \frac{\partial}{\partial t} \left( \frac{F_i}{4\pi r(1 - M_r)} \right) \right] e^{in\omega t} dt. \quad (\text{B.2})$$

Changing the variables back to retarded time and using  $dt = (1 - M_r)d\tau$  gives

$$c_n = \frac{\omega}{\pi} \int_0^{2\pi/\omega} \left[ \frac{x_i - y_i}{c_0 r} \frac{\partial}{\partial t} \left( \frac{F_i}{4\pi r(1 - M_r)} \right) \right] e^{in\omega(\tau+r/c_0)} d\tau \quad (\text{B.3})$$

and integrating by parts gives

$$c_n = \frac{\omega}{4\pi^2 r} \int_0^{2\pi/\omega} \left( \frac{in\omega F_r}{c_0} + \frac{F_i}{1 - M_r} \left[ \frac{-M_i}{r} + \frac{(x_i - y_i)}{r^2} M_r \right] \right) e^{[in\omega(\tau+r/c_0)]} d\tau \quad (\text{B.4})$$

where  $F_r = F_i(x_i - y_i)/r$  is the component of the force in the direction of the observer. The second term is important only in the acoustic near field, because of the additional factor  $r$  in the denominator. Thus, the result for the far-field becomes

$$c_n = \frac{\omega}{4\pi^2 r} \int_0^{2\pi/\omega} \left( \frac{in\omega F_r}{c_0} \right) e^{[in\omega(\tau+r/c_0)]} d\tau. \quad (\text{B.5})$$

To apply this model the fluctuating force field must be defined,

$$F_i = (-T, -D \sin \theta, D \cos \theta) \quad (\text{B.6})$$

where  $T$  is the thrust and  $D$  is the drag (torque). Note that the force on the air acts in the opposite direction to that on the blade. Now

$$r^2 = |\mathbf{r}|^2 = x^2 + y^2 + R^2 - 2yR \cos \theta \quad (\text{B.7})$$

and

$$x_i - y_i = (x, y - R \cos \theta, -R \sin \theta) \quad (\text{B.8})$$

from which

$$F_r = -xT/r - (yD/r) \sin \theta \quad (\text{B.9})$$

and applying the geometric far-field

$$\mathbf{r} = |x_i - y_i| \approx r_1 - (yR/r_1) \cos \theta \quad (\text{B.10})$$

where  $r_1$  is the distance from the observer to hub. Defining the complex cyclic thrust

$$T = \sum_{\lambda=-\infty}^{\infty} T_{\lambda} e^{-i\lambda\Omega t} \quad (\text{B.11})$$

and drag

$$D = \sum_{\lambda=-\infty}^{\infty} D_{\lambda} e^{-i\lambda\Omega t} \quad (\text{B.12})$$

forces on the blades by a complex Fourier series, where  $\Omega$  is the angular velocity of the rotor blades and  $\lambda$  gives the order of loading harmonic. The expression for the harmonics of the far-field sound radiation from the rotor is

$$c_n = \frac{in\Omega}{4\pi^2 c_0 r} \int_0^{2\pi/\omega} \sum_{\lambda=-\infty}^{\infty} \left( \frac{xT_{\lambda}}{r_1} + \frac{yD_{\lambda}}{r_1} \sin\theta \right) e^{[i(n-\lambda)\theta - in\alpha \cos\theta]} d\theta \quad (\text{B.13})$$

where  $\alpha = \Omega R y / c_0 r_1 = M y / r_1$ . Here  $M = \Omega R / c_0$  is the rotational Mach number of the point action of the force. The integrals can be identified as Bessel functions, using the expressions

$$\int_0^{2\pi} e^{i(n\theta - z \cos\theta)} d\theta = 2\pi i^{-n} J_n(z) \quad (\text{B.14})$$

and

$$\int_0^{2\pi} e^{i(n\theta - z \cos\theta)} \sin\theta d\theta = -2\pi i^{-n} \frac{n}{z} J_n(z). \quad (\text{B.15})$$

It can be evaluated directly to give the sound radiation from a single rotor blade as

$$c_n = \frac{in\Omega}{2\pi c_0 r_1} \sum_{\lambda=-\infty}^{\infty} (-i)^{n-\lambda} \left( \frac{xT_{\lambda}}{r_1} + \frac{n-\lambda}{n} \frac{D_{\lambda}}{M} \right) J_{n-\lambda} \left( \frac{nMy}{r_1} \right) \quad (\text{B.16})$$

where  $J_{n-\lambda}$  is the Bessel function of the first kind and the order  $n - \lambda$ . If  $B$  equally spaced rotor blades are present, harmonics that are not integral multiples of the number of blades are cancel. Thus, the final result for the complex magnitude of the  $m$ -th harmonic of noise radiated by the unsteady forces on the rotor is

$$c_m = \frac{imB^2\Omega}{2\pi c_0 r_1} \sum_{\lambda=-\infty}^{+\infty} (-i)^{mB-\lambda} \left( \frac{xT_{\lambda}}{r_1} - \frac{mB-\lambda}{mBM} D_{\lambda} \right) J_{mB-\lambda} \left( \frac{mBM y}{r_1} \right). \quad (\text{B.17})$$

The result can be rewritten in terms of ordinary Fourier coefficients.

$$\begin{aligned}
c_m = \frac{\Omega}{4\pi c_0 r_1} \sum_{\lambda=0}^{\infty} (-i)^{mB-\lambda-1} \left\{ \frac{mBx a_{\lambda T}}{r_1} \left( J_{mB-\lambda} + (-1)^\lambda J_{mB+\lambda} \right) \right. \\
+ \frac{imBx b_{\lambda T}}{r_1} \left( J_{mB-\lambda} - (-1)^\lambda J_{mB+\lambda} \right) \\
- \frac{a_{\lambda D}}{M} \left( (mB-\lambda) J_{mB-\lambda} + (n+\lambda) (-1)^\lambda J_{mB+\lambda} \right) \\
\left. - \frac{b_{\lambda D}}{M} \left( (mB-\lambda) J_{mB-\lambda} - (n+\lambda) (-1)^\lambda J_{mB+\lambda} \right) \right\}
\end{aligned} \tag{B.18}$$

where the arguments of all the Bessel functions is  $mBy/r_1$ , and  $a_{\lambda T}$ ,  $b_{\lambda T}$ ,  $a_{\lambda D}$ ,  $b_{\lambda D}$ , are ordinary Fourier coefficients of the fluctuating thrust and drag related to  $T_\lambda$  and  $D_\lambda$ . If the ordinary Fourier expression for thrust is

$$T = a_{0T} + \sum_{\lambda=1}^{\infty} a_{\lambda T} \cos \lambda \Omega t + b_{\lambda T} \sin \lambda \Omega t \tag{B.19}$$

then

$$T_\lambda = T_{\lambda R} + iT_{\lambda I} = (a_{\lambda T} + ib_{\lambda T})/2 \tag{B.20}$$

and

$$T_{-\lambda} = T_\lambda^* = T_{\lambda R} - iT_{\lambda I} = (a_{\lambda T} - ib_{\lambda T})/2 \tag{B.21}$$

so that the two Fourier series expressions are equivalent.

The  $J_{mB+\lambda}$  terms are negligible compared to the  $J_{mB-\lambda}$  terms, so that the simplified version of the model is

$$c_m = \frac{mB^2 \Omega}{4\pi c_0 r_1} \sum_{\lambda=0}^{\infty} (-i)^{mB-\lambda-1} \left\{ \frac{x}{r_1} (a_{\lambda T} + ib_{\lambda T}) - \frac{mB-\lambda}{mBM} (a_{\lambda D} + ib_{\lambda D}) \right\} J_{mB-\lambda}. \tag{B.22}$$

Assuming a reference frame with origin at the center of the hub, the complex amplitude of the acoustic pressure produced by the array in the far-field at the BPF harmonic of order  $mB$  can be expanded as the sum of radiation modes. The theoretical basis for tonal-noise analysis is the recognition of its modal structure, according to which the acoustic field of each tone can be expanded as an infinite sum of elementary waves. The mode radiation efficiency is determined by the Bessel-function factor.

The  $\lambda = 0$  mode defines the contribution due to steady loads, in reference frame of the propeller blade. In the special case when only steady forces exist on the rotor, this corresponds to the result obtained by Gutin [17]. It should be emphasized that only  $\lambda = 0$  mode relates to the total thrust and torque, which is of direct mechanical interest. Since at subsonic tip speeds,  $My/r_1$  is always less than unity, the corresponding Bessel factor can be very small. The intensity of the steady

loading noise is always zero at  $\theta = 0$  with strong peak just behind the rotation plane. If only the steady loading noise is considered, the tonal noise contribution shall be underestimated. At subsonic tip speeds, it is the unsteady blade forces that dominate the acoustic field, and not the steady Gutin noise. The unsteady blade loads generate a discrete frequency sound at the BPF and its harmonics. The acoustic field of each tone is the infinite sum of characteristic free-field radiation modes whose frequency is not necessary equal to the rate of rotation. The magnitude of each mode is proportional to the coefficients  $T_\lambda$  and  $D_\lambda$  of the Fourier series with a weighting factor defined by Bessel function. Each radiation mode rotates with an equivalent rotational speed.

As long as  $\lambda \neq mB$  the mode is called a spinning mode of radiation. A given spinning mode has a zero contribution to the far-field noise on the rotor axis and for another emission angle for which the squared bracket vanishes. Since each mode rotates at different frequency only the spinning modes of radiation with supersonic relative speed contribute significantly to the far-field sound. The specific case when  $\lambda = mB$  corresponds to the symmetric mode. This mode is the most efficient one in the sum of the related blade loading harmonic, because the Bessel factor is  $J_0$ , particularly at low tip Mach numbers. Most importantly, the symmetric mode is responsible for the on-axis radiation.

# Bibliography

- [1] A. Pasztor, FAA Projects fourfold increase in commercial drones by 2022, Wall Street Journal (2018).
- [2] A. W. Christian, R. Cabell, Initial investigation into the psychoacoustic properties of small unmanned aerial system noise, in: 23rd AIAA/CEAS Aeroacoustics Conference, 2017, p. 4051.
- [3] J. E. Ffowcs Williams, D. L. Hawkings, Sound generation by turbulence and surfaces in arbitrary motion, Philosophical Transactions of the Royal Society of London. Series A, Mathematical and Physical Sciences 264 (1151) (1969) 321–342.
- [4] M. Lowson, Basic mechanisms of noise generation by helicopters, v/stol aircraft and ground effect machines, Journal of Sound and Vibration 3 (3) (1966) 454–466.
- [5] M. Lowson, J. Ollerhead, A theoretical study of helicopter rotor noise, Journal of Sound and Vibration 9 (2) (1969) 197–222.
- [6] C. Morfey, Rotating blades and aerodynamic sound, Journal of Sound and Vibration 28 (3) (1973) 587–617.
- [7] J. Brandt, M. Selig, Propeller performance data at low reynolds numbers, in: 49th AIAA aerospace sciences meeting, 2011, pp. 2011–1255.
- [8] J. Brandt, R. Deters, S. M. Ananda, G.K., Uiuic propeller database, <http://m-selig.ae.illinois.edu/props/propDB.html>, university of Urbana Champaign (2005).
- [9] N. Intaratep, W. N. Alexander, W. J. Devenport, S. M. Grace, A. Dropkin, Experimental study of quadcopter acoustics and performance at static thrust conditions, in: 22nd AIAA/CEAS Aeroacoustics Conference, 2016, p. 2873.
- [10] N. Zawodny, D. Boyd Jr, C. Burley, Acoustic characterization and prediction of representative, small-scale rotary-wing unmanned aircraft system components (2016).

- [11] A. Cambray, E. Pang, D. Rezgui, M. Azarpeyvand, S. A. Showkat Ali, Investigation towards a better understanding of noise generation from uav propellers, in: 2018 AIAA/CEAS Aeroacoustics Conference, 2018, p. 3450.
- [12] C. Tinney, J. Sirohi, Multirotor drone noise at static thrust, *AIAA Journal* (2018) 1–11.
- [13] J. H. Stephenson, D. Weitsman, N. S. Zawodny, Effects of flow recirculation on unmanned aircraft system (uas) acoustic measurements in closed anechoic chambers, *The Journal of the Acoustical Society of America* 145 (3) (2019) 1153–1155.
- [14] D. L. Huff, B. S. Henderson, Electric motor noise for small quadcopters: Part 1–acoustic measurements, in: 2018 AIAA/CEAS Aeroacoustics Conference, 2018, p. 2952.
- [15] J. F. Williams, D. Hawkings, Sound generation by turbulence and surfaces in arbitrary motion, *Phil. Trans. R. Soc. Lond. A* 264 (1151) (1969) 321–342.
- [16] K. S. Brentner, F. Farassat, Modeling aerodynamically generated sound of helicopter rotors, *Progress in Aerospace Sciences* 39 (2-3) (2003) 83–120.
- [17] L. Gutin, On the sound field of a rotating propeller, *Physiks Zeitschrift der Sowjetunion, Band A Heft, 1* (1936).
- [18] N. Curle, The influence of solid boundaries upon aerodynamic sound, *Proc. R. Soc. Lond. A* 231 (1187) (1955) 505–514.
- [19] V. P. Blandeau, P. F. Joseph, Validity of amiet’s model for propeller trailing-edge noise, *AIAA journal* 49 (5) (2011) 1057–1066.
- [20] S. Sinayoko, M. Kingan, A. Agarwal, Trailing edge noise theory for rotating blades in uniform flow, in: *Proc. R. Soc. A, Vol. 469*, The Royal Society, 2013, p. 20130065.
- [21] W. K. Blake, *Mechanics of flow-induced sound and vibration*, 2nd edition. Cambridge, MS, Academic Press, 2017.
- [22] M. E. Goldstein, *Aeroacoustics*, New York, McGraw-Hill International Book Co., 1976.
- [23] S. Glegg, W. Devenport, *Aeroacoustics of low Mach number flows: fundamentals, analysis, and measurement*, Academic Press, 2017.
- [24] S. Sinayoko, M. Kingan, A. Agarwal, Trailing edge noise theory for rotating blades in uniform flow, *Proceedings of the Royal Society A: Mathematical, Physical and Engineering Sciences* 469 (2157) (2013) 20130065.

- [25] R. Amiet, Noise due to turbulent flow past a trailing edge, *Journal of sound and vibration* 47 (3) (1976) 387–393.
- [26] R. Amiet, Effect of the incident surface pressure field on noise due to turbulent flow past a trailing edge, *Journal of Sound and Vibration* 57 (2) (1978) 305–306.
- [27] T. F. Brooks, D. S. Pope, M. A. Marcolini, Airfoil self-noise and prediction, NASA Reference Publication 1218 (1989).
- [28] J. F. Williams, L. Hall, Aerodynamic sound generation by turbulent flow in the vicinity of a scattering half plane, *Journal of fluid mechanics* 40 (4) (1970) 657–670.
- [29] R. Amiet, Acoustic radiation from an airfoil in a turbulent stream, *Journal of Sound and Vibration* 41 (4) (1975) 407–420.
- [30] J. Giez, L. Vion, M. Roger, S. Moreau, Effect of the edge-and-tip vortex on airfoil selfnoise and turbulence impingement noise, in: 22nd AIAA/CEAS Aeroacoustics Conference, 2016, p. 2996.
- [31] T. Brooks, D. Pope, M. Marcolini, Airfoil self-noise and prediction (1989).
- [32] T. Chong, P. Joseph, M. Kingan, An investigation of airfoil tonal noise at different reynolds numbers and angles of attack, *Applied Acoustics* 74 (1) (2013) 38–48.
- [33] T. P. Chong, P. Joseph, ‘ladder’ structure in tonal noise generated by laminar flow around an airfoil, *The Journal of the Acoustical Society of America* 131 (6) (2012) EL461–EL467.
- [34] E. Arcondoulis, C. Doolan, A. Zander, L. Brooks, A review of trailing-edge noise generated by airfoils at low to moderate reynolds number., *Acoustics Australia* 38 (3) (2010).
- [35] M. Merchant, L. S. Miller, Propeller performance measurement for low reynolds number uav applications, Vol. 1127, 2006, p. 2006.
- [36] T. Carroll, I. George, G. Bramesfeld, K. Raahemifar, Design optimization of small rotors in quad-rotor configuration, in: AIAA, 2016, p. 1788.
- [37] T. Geyer, E. Sarradj, J. Nowigk, Design and construction of a test stand for noise measurements on model propellers, *Fortschritte der Akustik-AIA-DAGA* 1891 (1888) 2013.
- [38] G. Sinibaldi, L. Marino, Experimental analysis on the noise of propellers for small uav, *Applied Acoustics* 74 (1) (2013) 79–88.

- [39] P. Welch, The use of fast fourier transform for the estimation of power spectra: a method based on time averaging over short, modified periodograms, *IEEE Transactions on audio and electroacoustics* 15 (2) (1967) 70–73.
- [40] M. Feldman, *Hilbert transform applications in mechanical vibration*, John Wiley & Sons, 2011.
- [41] G. J. Leishman, *Principles of helicopter aerodynamics with CD extra*, Cambridge university press, 2006.
- [42] W. Zhou, Z. Ning, H. Li, H. Hu, An experimental investigation on rotor-to-rotor interactions of small uav propellers, in: *35th AIAA applied aerodynamics conference*, 2017, p. 3744.
- [43] H. Lee, D.-J. Lee, Rotor interactional effects on aerodynamic and noise characteristics of a small multicopter unmanned aerial vehicle, *Phys. Fluids* 32 (4) (2020) 047107.
- [44] E. Zwicker, H. Fastl, *Psychoacoustics: Facts and models*, Vol. 22, Springer Science & Business Media, 2013.
- [45] S. R. More, *Aircraft noise characteristics and metrics*, Purdue University, 2010.
- [46] W. M. Siebert, Frequency discrimination in the auditory system: Place or periodicity mechanisms?, *Proceedings of the IEEE* 58 (5) (1970) 723–730.
- [47] M. G. Heinz, H. S. Colburn, L. H. Carney, Evaluating auditory performance limits: I. one-parameter discrimination using a computational model for the auditory nerve, *Neural computation* 13 (10) (2001) 2273–2316.
- [48] M. Furst, Cochlear model for hearing loss, in: *Update On Hearing Loss*, IntechOpen, 2015.
- [49] E. V. Loureiro, N. L. Oliveira, P. H. Hallak, F. de Souza Bastos, L. M. Rocha, R. G. P. Delmonte, A. C. de Castro Lemonge, Evaluation of low fidelity and cfd methods for the aerodynamic performance of a small propeller, *Aerospace Science and Technology* 108 (2021) 106402.
- [50] D. Casalino, E. Grande, G. Romani, D. Ragni, F. Avallone, Definition of a benchmark for low reynolds number propeller aeroacoustics, *Aerospace Science and Technology* (2021) 106707.
- [51] W. J. M. Rankine, On the mechanical principles of the action of propellers, *Transactions of the Institution of Naval Architects* 6 (1865) 13–39.

- [52] R. E. Froude, On the part played in propulsion by differences of fluid pressure, *Trans. Inst. Naval Architects* 30 (1889) 390.
- [53] S. Drzewiecki, *Théorie générale de l'hélice: hélices aériennes et hélices marines*, Gauthier-Villars et cie., 1920.
- [54] H. Glauert, *The elements of aerofoil and airscrew theory*, Cambridge University Press, 1983.
- [55] T. Theodorsen, Theory of propellers, *Skipsmodelltankens meddelelse nr. 33*, April 1954 (1954).
- [56] E. Larrabee, Propellers of minimum induced loss, and water tunnel tests of such a propeller, *Proceedings of the NASA, Industry, University, General Aviation Drag Reduction Workshop, University, General Aviation Drag Reduction Workshop, NASA Conference Publication, Lawrence, Kansas 273–293*.
- [57] C. Adkins, R. LIEBECK, Design of optimum propellers, in: *21st Aerospace Sciences Meeting*, 1983, p. 190.
- [58] M. Drela, Xfoil: An analysis and design system for low reynolds number airfoils, in: *Low Reynolds number aerodynamics*, Springer, 1989, pp. 1–12.
- [59] C. N. Adkins, R. H. Liebeck, Design of optimum propellers, *Journal of Propulsion and Power* 10 (5) (1994) 676–682.
- [60] O. Gur, A. Rosen, Comparison between blade-element models of propellers, *The Aeronautical Journal* 112 (1138) (2008) 689–704.
- [61] H. Glauert, Airplane propellers, in: *Aerodynamic theory*, Springer, 1935, pp. 169–360.
- [62] I. H. Abbott, A. E. Von Doenhoff, *Theory of wing sections dover publications*, New York (1959).
- [63] G. J. J. B. A. P. Selig, M. S., P. Giguere, *Summary of Low-Speed Airfoil Data, Vol. 1*, SoarTech Publications, 1995.
- [64] L. C. A. G. P. N. C. N. Selig, M. S., J. J. Guglielmo, *Summary of Low-Speed Airfoil Data, Vol. 2*, SoarTech Publications, 1996.
- [65] L. C. A. G. P. N. C. N. Selig, M. S., J. J. Guglielmo, *Summary of Low-Speed Airfoil Data, Vol. 3*, SoarTech Publications, 1998.

- [66] L. A. Viterna, R. D. Corrigan, Fixed pitch rotor performance of large horizontal axis wind turbines, in: NASA Lewis Research Center: Energy Production and Conversion Workshop, Cleveland, OH, United States January, Vol. 1, 1982.
- [67] B. Montgomerie, Methods for root effects, tip effects and extending the angle of attack range to  $\{\pm\}$  180 deg., with application to aerodynamics for blades on wind turbines and propellers (2004).
- [68] C. Lindenburg, Investigation into rotor blade aerodynamics, Energy research Centre of the Netherlands (ECN) Wind Energy publication, ECN-C-03-025 (2003).
- [69] D. A. Spera, Models of lift and drag coefficients of stalled and unstalled airfoils in wind turbines and wind tunnels (2008).
- [70] C. C. Critzos, H. H. Heyson, R. W. Boswinkle Jr, Aerodynamic characteristics of naca 0012 airfoil section at angles of attack from 0 deg to 180 deg, Tech. rep., NATIONAL AERONAUTICS AND SPACE ADMINISTRATION WASHINGTON DC (1955).
- [71] C. Ostowari, D. Naik, Post-stall wind tunnel data for naca 44xx series airfoil sections, Tech. rep., Texas A and M Univ., College Station (USA). Dept. of Aerospace Engineering (1985).
- [72] A. M. O. Smith, Transition, pressure gradient and stability theory, Douglas Aircraft Co., Report ES 26388 (1956).
- [73] J. Van Ingen, A suggested semi-empirical method for the calculation of the boundary layer transition region, Technische Hogeschool Delft, Vliegtuigbouwkunde, Rapport VTH-74 (1956).
- [74] L. M. Mack, Transition and laminar instability, Jet Propulsion Laboratory Publication 78 (1977).
- [75] A. F. Deming, Propeller rotation noise due to torque and thrust, The Journal of the Acoustical Society of America 12 (1) (1940) 173–182.
- [76] M. Lowson, The sound field for singularities in motion, Proceedings of the Royal Society of London. Series A. Mathematical and Physical Sciences 286 (1407) (1965) 559–572.